Title: A three-dimensional Distributed Acoustic Sensing array to monitor local seismicity

Authors: Jerome Azzola[1], Emmanuel Gaucher[1]

[1]Kalrsruhe Institute of Technology (KIT), Institute of Applied Geosciences (AGW) Department of Geothermal Energy and Reservoir Technology, Adenauerring 20b, 76131, Karlsruhe (Germany)

Corresponding author: Jerome Azzola, jerome.azzola@kit.edu

Abstract

Distributed Acoustic Sensing (DAS) has emerged as a valuable complement to conventional seismic monitoring techniques. By converting fiber-optic cables into dense arrays of virtual sensors, DAS enables the application of standard large-array processing methods. However, its directional sensitivity – limited to strain measurements along the fiber axis – may restrict its potential for full wavefield analysis. To address this limitation, we investigate the capabilities of DAS on a fiber-optic cable installed both horizontally, near the surface, and vertically, in a borehole, thereby creating a so-called 3D-DAS array. The survey was carried out in the southern Munich region (Germany) to monitor local seismicity associated with nearby deep geothermal operations. In this study, we present the data acquisition setup and describe a processing workflow developed to characterize source and wavefield parameters of seismic events from DAS recordings. The workflow is illustrated using a nearby M_w = 0.48 seismic event. Taking advantage of the configuration of the fiber optic cable, we demonstrate that the 3D-DAS array enables estimation of the wavefield back-azimuth, incidence angle and slowness, and compare these results with those provided by a local network of seismometers.

In addition, seismic source parameters, including seismic moment and stress drop, are estimated from DAS data acquired in the 250-meter-deep vertical well. These parameters are derived after converting strain-rate to ground motion, a process quantitatively validated using a co-located three-component broadband seismometer. The results and waveform evaluation demonstrate that the 3D-DAS array provides reliable and comprehensive measurements, independently of the existing local seismic network.

Key words: Distributed acoustic sensing, Earthquake monitoring and test-ban treaty verification, Induced seismicity, Seismic instruments, Earthquake source observation.

1 Introduction

Distributed Acoustic Sensing (DAS) turns fiber optic cable (FOC) into an array of sensors capable of measuring strain-rate (SR) of its surrounding material. With DAS, an Interrogation Unit (IU) sends laser pulses through the fiber and analyses changes in the Rayleigh backscattered light. Pioneering research by Dakin (1990) and Taylor and Lee (1993) demonstrate the potential of coherent Rayleigh backscattering to measure temporal variations in SR along fiber segments functioning like individual gauges of fixed length (or gauge length, GL). The resulting time series are referenced to sensing points (SP) centered on each gauge, and a regular SP spacing along the fiber provides spatially resolved measurements. The use of short laser pulses also allows DAS system to capture a wide bandwidth of frequencies. DAS can thus capture seismic vibrations ranging from millihertz to tens of kilohertz with high spatial resolution, provided that strain in the surrounding medium is effectively transmitted to the optical fiber (Lindsey *et al.* 2020; Paitz *et al.* 2021; Zhai *et al.* 2025).

Since its pioneering research, the technology has significantly advanced towards increased sensitivity (Hartog 2017) and has been adopted across a broad spectrum of geophysical applications (e.g., Hartog, 2017; Lellouch and Biondi, 2021; Li et al., 2021), while persistent challenges continue to drive future research directions (Markom *et al.* 2025). The high spatial density of SP and the inherent array or antenna nature makes DAS well-suited for applying array processing techniques developed in passive or active seismics, in particular for data de-noising (Isken *et al.* 2022), seismic event detection (Lellouch *et al.* 2019; Nayak *et al.* 2021) or seismic event location (Verdon et al., 2020; Zhan, 2020; Lentas et al., 2023). However, processing capabilities can vary depending on the cable trajectory, primarily because the sensitivity is limited to the longitudinal deformation of the fiber.

In the Munich region (Germany), DAS on a vertical FOC, cemented behind the casing of a geothermal injection well, contributed to local monitoring efforts (Azzola et al., 2023; Azzola and Gaucher, 2024). The authors demonstrate that this vertical (linear) antenna of SPs enhances the sensitivity and density of the monitoring network, contributing to the detection and description of local seismic events. However, studying the full directionality of the wavefield and resolving seismic event hypocenters cannot be achieved from this vertical antenna on its own. In contrast, FOCs installed along multiple directions in the horizontal plane would provide complementary information. Nayak et al. (2021) demonstrate the capabilities of beamforming on a dark-fiber to detect weak seismic events at a regional scale. Lentas et al (2023) locate a M_L=3.4 regional seismic event near Athens, Greece, using a commercial FOC deployed as a controlled seismic array. At the local scale, Nishimura et al. (2021) locate the source of volcanic earthquakes using DAS with a 14 km-long FOC deployed along a mountain road. Studies by van den Ende and Ampuero (2021), Muñoz and Soto (2022) or Lentas et al. (2023) nevertheless outline potential challenges

related to high noise level and partial lack of coherency in DAS signals, limiting the array capabilities to resolve the directionality of the wave field. Additionally, variations in the SPs response along the FOC, caused by potential heterogeneities in Earth's structure or differences in cable coupling, could introduce additional challenges.

Combined vertical-horizontal DAS layouts remain relatively uncommon, yet they offer clear advantages in terms of azimuthal coverage and wavefield characterization. Verdon *et al.* (2020) highlight the benefits of a L-shaped borehole deployment to enhance azimuthal coverage and improve the characterization of wavefields for microseismic monitoring. The PoroTomo experiment is another notable case study, in which a large near-surface DAS array was used alongside borehole DAS (K. Feigl *et al.* 2016, 2018). Seismicity from the nearby Brady geothermal field has been primarily studied using the surface DAS array (Z. Li and Zhan 2018; Lv *et al.* 2023).

The present study introduces a seismic monitoring installation equipped with DAS where the FOC, both cemented in a vertical well and buried near-surface in a loop configuration, is configured to provide three-dimensional sensing capabilities. The so-called 3D-DAS array, whose layout accommodates the spatial constraints of a residential neighborhood, is designed to characterize low-magnitude (ML < 2) seismicity that may be induced by local geothermal operations, with particular focus on two geothermal fields located about 4 km away. The aim of this study is to demonstrate that SR recordings collected in multiple horizontal directions and along the vertical antenna enable robust estimation of wavefield- and source-parameters. We present a comprehensive workflow for routine analysis of the seismic wavefield directionality (back-azimuth, incidence and slowness components) and of seismic source parameters, including hypocenter, seismic moment, moment magnitude and stress drop. A collocated 3-component (3C) broadband seismometer, which belongs to a local network of

seismometers, provides an independent reference for validating the SR data and processing results.

In the following, we first detail the context in which the seismic monitoring installation, including the 3D-DAS array, was designed and implemented and how the data were acquired. Then, we present the processing steps applied to the DAS recordings to obtain the directionality of the seismic wave field and the seismic source parameters. This is illustrated with a local seismic event located in the monitoring zone. Then, the quality of the surface and borehole SR measurements is controlled by comparison with the collocated broadband 3C-seismometer. Finally, the sensitivity and resolution of the 3D-DAS array is discussed in the light of the FOC geometry and the analysis of a larger catalog of seismic events that occurred outside the monitoring zone.

2 Data acquisition set-up

2.1 Monitoring context

The study area is situated within the German Molasse Basin, a foreland basin formed by the alpine orogeny during the Oligocene and Miocene (Hartmann et al., 2016). The Malm carbonates of the Molasse Basin are prime targets for geothermal heat production due to their favorable reservoir properties and the high temperatures of the fluid found at 3 to 4-km depth (Schulz and Jobmann, 1989; Dussel et al., 2016; Farquharson et al., 2016). An increasing number of energy companies in both the northern and southern parts of Munich operate the porous Malm carbonates to supply district heating networks and contribute to Munich region's transition towards renewable heat supply (Cröniger *et al.* 2022). Currently, over twenty geothermal energy projects are operational in the Greater Munich area, with an additional nine projects in development (Bundesverband Geothermie 2024).

Observations of induced seismicity have been documented in the area, although geothermal operations target hydrothermal systems supported by a porous matrix (Kraft *et al.* 2009; Megies and Wassermann 2014; Seithel *et al.* 2019). With the growth of the geothermal energy production, local and site-specific seismic monitoring plays a crucial role in the sustainable development of the energy sector (Azzola *et al.* 2023; Keil *et al.* 2023).

The seismic monitoring installation of interest is located midway between the geothermal site of Pullach im Isartal and the future Pullach Süd project (Bundesverband Geothermie 2024), in the village of Buchenhain (Figure 1, label BUCH). Its objective is to detect and characterize seismic sources from the Malm reservoir within a monitoring zone of roughly 4 km radius, including the Pullach Süd project and the Pullach geothermal field. The installed instruments consolidate the local seismic network (Department of Earth and Environmental Sciences, Geophysical Observatory, University of Munchen, 2001), which includes ten 3C-broadband seismometers monitoring continuously the study area (Figure 1a).

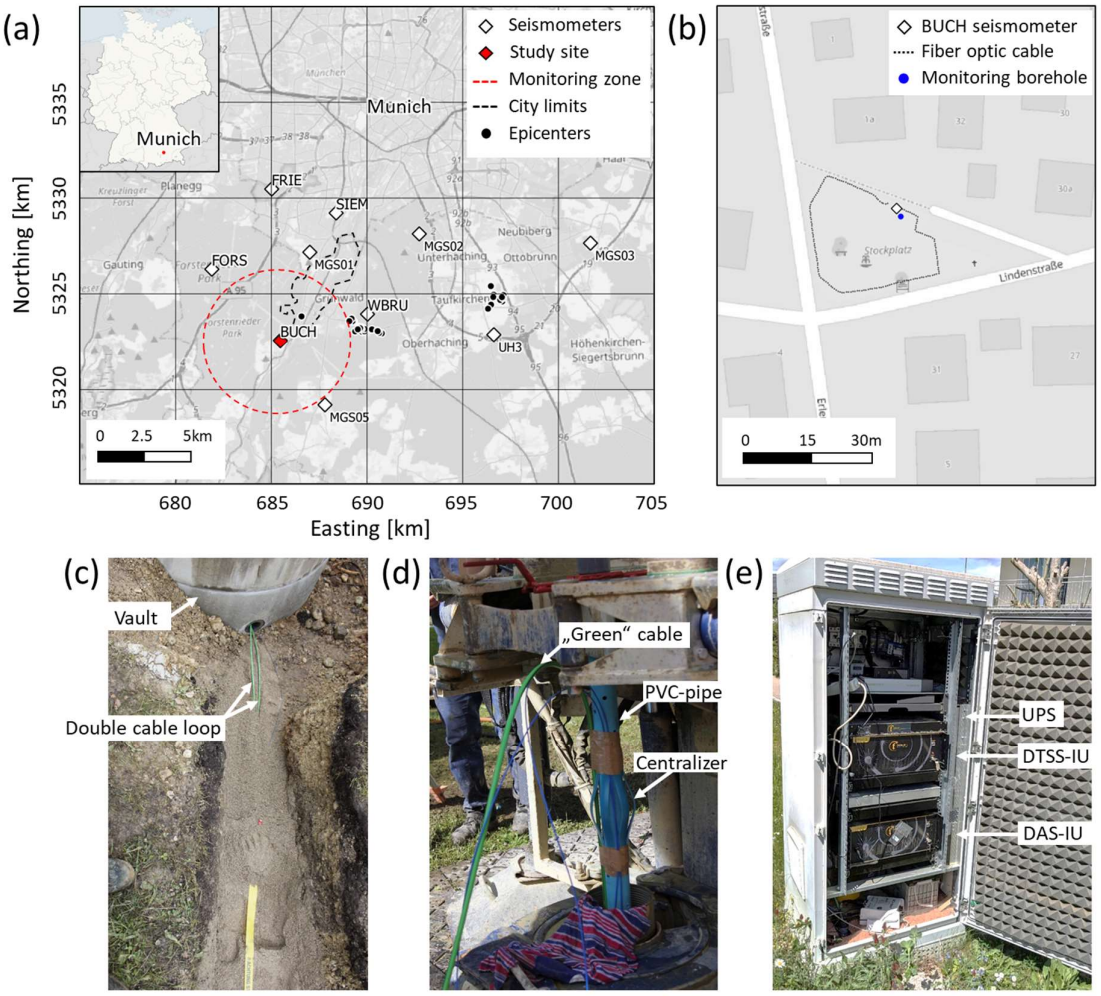

Figure 1: (a): Overview of the study area, in southern Munich (Germany), with the location of seismometers (diamonds) monitoring continuously the area around the city of Pullach im Isartal (dashed line). The red diamond labeled BUCH indicates the location of the monitoring installation under study and the red dash line the targeted monitoring zone. The black dots show the epicenters of the seismic events detected during the period of continuous data acquisition analyzed here, from March 25, 2022, to December 31, 2023. Coordinate system: WGS 84/UTM 32 (EPSG 32632). (b): Focus on the center of the Buchenhain village, where the instruments are installed, with the trajectory of the near-surface section of the FOC (black curve), the position of the vertical well (blue dot) and of the 3C-broadband

seismometer (white diamond). (c): FOCs exiting the vault and being laid down in the trench before burying. The green FOC is used in this study. (d): Deployment of FOCs in the well, prior to cementation. The cables are attached to the cementation PVC-pipe, which is kept centralized using bow-spring centralizers. (e): Electrical cabinet used to store the acquisition equipment on the surface.

2.2 Monitoring installation set-up

The monitoring installation is located in a small park within a residential area (Figure 1b). Appendix A includes additional pictures of the installation and its surroundings. The sensing instruments include a 3C-broadband seismometer (Trillium Compact TC120), which is installed on the floor of a 2-m deep vault. The FOC (green cable in Figure 1c) is dedicated to distributed fiber optic sensing. It has a stiff jacket containing tight-buffered single mode fibers, which is appropriate for DAS (Willis *et al.* 2021), and loose fibers for Distributed Strain and Temperature Sensing (not the focus of this work). The FOC was deployed in two sections, one near the surface and the other one in a vertical well. Both sections are interconnected in a junction box located inside the vault.

For the near-surface section, the cable is laid in a 90-cm deep trench, on a layer of sand, then covered with sand and finally buried under the overburden (Figure 1c). This ensures suitable coupling with the surrounding formation, which is a key factor to conduct high-quality DAS measurements (Munn *et al.* 2017; Willis *et al.* 2021). The FOC follows the outer edges of the park, forming an approximately 90-m-long loop. The cable loop was doubled, with both cable stretches laid in parallel, to provide redundancy in the SP and increase the effective spatial sampling along the cable trajectory.

With the FOC layout established, the characterization of SPs includes their geo-referencing and the determination of the recording azimuth. The mapping of SPs is described in

Appendix B. We use the surface redundancy to combine parallel loops into a single, higher-resolution virtual array. Because the trenched FOC follows a complex trajectory, the cable azimuth can vary over each GL. We characterize the recording azimuth of each SP by calculating the average FOC azimuth over the corresponding GL. The coordinates and azimuths of the DAS SPs are indicated in Appendix B.

For the vertical section of the FOC, the cable was clamped with tape, every 4 m, to a DN50 PVC cementation pipe that was centralized every 8 m and lowered in the 250-m vertical well. The bow-spring centralizers were not rotating and the FOC was routed in-between their arms (Figure 1d). The lower end of the cable was sealed with epoxy resin to avoid fiber deterioration and protected by a first centralizer. Cementation was performed from bottom to top of the well. A cable-through diverts the FOC from the top of the well to the vault, where it is connected to the surface loop in the junction box.

The whole acquisition system is installed in an electrical cabinet (Figure 1e) connected to the surface loop. This cabinet includes an uninterruptible power supply device that powers the DAS IU, a Febus Optics A1R, an external hard drive for local storage of DAS data, a router for remote access to the system and the seismometer data logger. The cabinet is ventilated to regulate its inner temperature and is insulated to ensure minimal noise disturbance of the neighborhood. With only the electrical cabinet being visible from the surface, the seismic monitoring installation has a small visual impact.

2.3 Data acquisition

DAS data were recorded continuously from March 25, 2022, to December 31, 2023. A 500 Hz sampling rate was used for data acquisition (see Appendix C for all recording parameters). SR is recorded over a 20-m gauge-length (GL), which corresponds to the longest straight segment of the surface loop. As suggested by Dean et al. (2017) or Näsholm et al. (2022), this

parameter is also well suited for monitoring local seismic events characterized by signal frequencies of 30 to 50 Hz and occurring in media with seismic velocities of approximately 2000 m s^{-1}. We use a nominal SP spacing of 10 m along the FOC. On the near-surface section, the two cable loops running in parallel in the trench reduce the effective inter-channel spacing. Hence, the spacing between two successive SPs along the cable in this section is 4 or 6 m, as summarized in Table B2.

Seismic data was also recorded continuously during the period of interest on the network of seismometers shown in Figure 1a, which includes the 3C-broadband seismometer installed at the site of the 3D-DAS array (SEED code BUCH.HL*). The sampling frequency was 250 Hz and data were transferred continuously via mobile network, in contrast to the DAS recordings, which were stored locally.

3 Seismic processing workflow

This section details the processing steps applied to DAS and seismometer recordings, which are also summarized in Figure 2. The resulting analysis for a seismic event occurring within the monitoring zone is presented in Section 4.

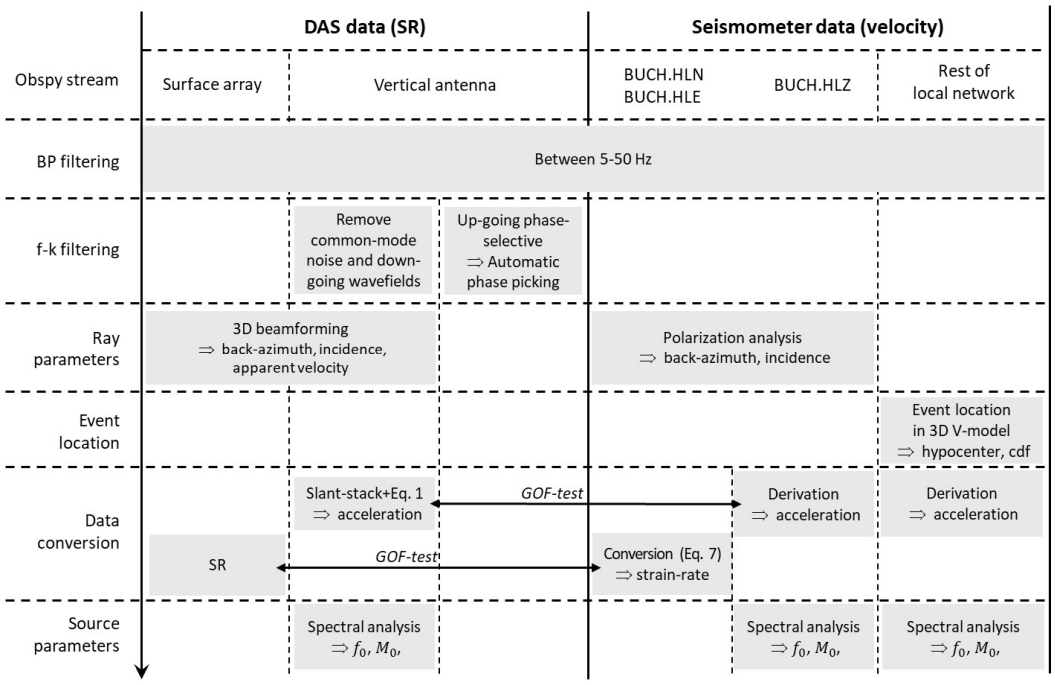

Figure 2: Overview of the workflow applied to both DAS and seismometer data. The processing steps presented in each row are arranged sequentially from top to bottom. The gray boxes indicate how each step is implemented for the different data types and components, where applicable, with intermediate outputs shown after each arrow.

3.1 Pre-processing

Once recorded by the IU, DAS data files (HDF5 format) are loaded in memory and reshaped as an Obspy stream (Beyreuther *et al.* 2010) to facilitate standard seismological processing. During pre-processing, we extract DAS traces from the surface loops and the vertical well (first row in Figure 2), assign their geographic positions, and generate associated metadata. The Obspy streams of the DAS and seismometer channels are initially filtered between 5 and 50 Hz using a forward and backward fourth-order Butterworth band-pass filter (Butterworth 1930).

3.2 Vertical antenna processing

The (vertical) alignment of the in-well SPs enables the use of antenna processing technique for further data filtering and conversion, thereby supporting the estimation of source parameters (rows 3, 6 and 7 in Figure 2).

First, velocity filters in the frequency-wavenumber (f-k) domain (Isken *et al.* 2022) can be configured to suppress various types of perturbations in the DAS datasets. One goal is to attenuate coherent, laser-induced noise, observed as signals propagating with infinite apparent velocity along the fiber (i.e., along the zero-wavenumber axis in the f–k domain), commonly referred to as common-mode noise (Zhirnov *et al.* 2019). The velocity filter is also used to remove down-going wavefields associated to surface noise or wave reflections, typically observed in the positive frequency/negative wavenumber or negative frequency/positive wavenumber quadrants in the f-k domain. This facilitates the study of up-going wavefields typical of seismic events located below the antenna (Azzola *et al.* 2023). As an extension of this approach, a narrow velocity filter tuned to the apparent velocities of the P- and/or S-wave fronts is applied to isolate specific phases and thereby enhance their signal-to-noise ratio (SNR), following Azzola and Gaucher (2024). Subsequently, P-wave onsets are automatically picked using a STA/LTA detector, with further refinement based on the earliest zero-crossing of the trace exhibiting the highest SNR. This refined pick is then propagated to all remaining traces through waveform cross-correlation.

Second, under the assumption of plane-wave propagation along the vertical fiber, we use the dense spatial sampling along the vertical antenna and resulting coherence (or semblance) of adjacent traces to convert SR to ground motion, here, acceleration. Equation (1) relates strain-rate ($\dot{\varepsilon}_z(t)$) and acceleration ($a_z(t)$) time series, recorded along the vertical direction z, using the apparent phase slowness s_z, following the formulation introduced by Daley *et al.* (2016)

and Wang *et al.* (2018), or used by Lior *et al.* (2021). A detailed equation derivation is provided in Appendix D.

$$a_z(t) = \frac{1}{s_z} \cdot \dot{\varepsilon}_z(t) \tag{1}$$

Instead of applying Equation (1) with an apparent phase slowness constant in time, we estimate the temporal variations at each trace from a slant-stack transformation. Rooted in exploration seismology, this transformation leverages dense, regularly spaced receiver arrays and coherent plane wave propagation (Schultz and Claerbout 1978; Taner *et al.* 1979). The method, proposed by Lior et al. (2021) and applied for example by Lior et al. (2023) or Azzola and Gaucher (2024), is data-driven and can adapt to localized changes in apparent velocity. It is repeated at every SP, which is treated as the pivot of a symmetrical array of 2*D*+1 traces. For each temporal sample, the traces within this coherence-window are time-shifted according to a range of trial apparent slowness values s_i. The coherence of neighboring traces is then quantified from Equation (2), where the difference between z_j and z_0 denotes the distance between SP j and the pivot trace, $g(t)$ represent the seismic traces. The Hilbert transform $h(t)$ is introduced to capture phase information and allow robust coherence estimation even at zero-crossings, where amplitude alone would underestimate coherence.

$$\mathrm{coh}(s_i, t) = \frac{\left[\left[\sum_{j=-D}^{D} g(t+s_z \cdot (z_j - z_0))\right]^2 + \left[\sum_{j=-D}^{D} h(t+s_z \cdot (z_j - z_0))\right]^2\right]}{[2D+1] \cdot \left[\sum_{j=-D}^{D} g(t+s_z \cdot (z_j - z_0))^2 + h(t+s_z \cdot (z_j - z_0))^2\right]} \tag{2}$$

At a given time, the slowness yielding the highest coherence characterizes the most-coherent local plane wave. To avoid sharp variations and preserve the meaningful dynamics in the

estimated slowness time-series, we apply a moving average filter with a window size set to the shortest period of interest in the signal. We use a 100-m wide coherence window (D = 5) in Equation (2) to ensure sufficiently correlated traces contribute (Section 4.2), noting that the window size must remain within the signal's spatial coherence while an increase in its length improves slowness resolution. In addition, using Equation (2) across all SPs and time steps estimates a coherence amplitude over every data point in the time-offset DAS recordings, which, when used as a weight, can improve SNR by separating coherent signals from random noise (Schwarz, 2019).

After conversion, acceleration traces can finally be used as input for seismic source parameter inversion by fitting an omega-squared model to the observed acceleration spectra. The synthetic acceleration spectrum $\ddot{\Omega}(f)$ is described as a function of frequency by Anderson and Hough (1984) (Equation 3), where Ω_0 is the low-frequency displacement spectrum plateau, f_0 is the source corner frequency and f_k is the attenuation corner frequency controlling the behavior at high frequencies.

$$\ddot{\Omega}(f) = 2\pi f^2 \cdot \frac{\Omega_0}{1+(f/f_0)^2} \cdot \exp(-f/f_k) \quad (3)$$

For local seismicity, observed acceleration spectra are computed using 0.8-second-long windows starting at the P-wave onset time, and are used to estimate Ω_0 and f_0. Scalar seismic moments, M_0, are computed from Ω_0 using the fault dynamic model proposed by Madariaga (1976). Moment magnitudes, M_W, are subsequently estimated according to Hanks and Kanamori (1979). We evaluate the stress drop ΔS assuming a circular fault model, as proposed by Eshelby and Peierls (1957) and dynamically modeled by Madariaga (1976):

$$\Delta S = \frac{7}{16} \cdot M_0 \cdot \left(\frac{f_0}{k\, V_S}\right)^3 \quad (4)$$

In Equation (4), f_0 is the corner frequency. In the absence of site-specific studies, we adopt the empirical scaling factor k proposed by Madariaga (1976) for a circular crack model expanding at a rupture velocity of $0.9 \cdot V_S$. To calculate source radii from observed corner frequencies, this study used k = 0.32 and k = 0.21 for P- and S-waves, respectively.

Equations (3) and subsequent source parameter estimations are applied to the acceleration time-series obtained at each SP in the vertical well. As shown in Figure 2, they are likewise applied after differentiating particle velocity data from each seismometer of the local seismological network, which supports the results comparison in Section 4.

In contrast to other approaches that estimate earthquake magnitudes from DAS data using empirical scaling relations (e.g., Yin *et al.* 2023), the proposed methodology does not rely on calibrated scaling factors. The approach was previously applied by Azzola and Gaucher (2024) in borehole DAS-monitoring of a geothermal field, where the comparison with seismometer data confirmed the reliability of the DAS results.

3.3 3D-DAS array processing

The distinctive feature of the 3D-DAS array is its ability to combine recordings from gauges oriented in different azimuths and inclinations (fourth row in Figure 2). We use a 3D delay-and-sum beamforming algorithm (e.g., Johnson and Dudgeon, 1993) formulated in the time-domain to jointly process the SR traces from the surface loops and the vertical well, assuming incident plane waves. Hence, we estimate ray parameters, including the back azimuth (BAZ, ϕ), incidence angle (INC, i) and propagation velocity of the wave field close to the FOC (v_c). For a set of candidate parameters, the algorithm uses Equation (5) to calculate the time delay

τ_j between a SP j with coordinates (x_j, y_j, z_j) and a reference point, taken as the position of the wellhead. Details on the equation derivation are provided by Schweitzer et al. (2012):

$$\tau_j = \frac{-x_j \cdot \sin i \cdot \sin \phi - y_j \cdot \sin i \cdot \cos \phi + z_j \cdot \cos i}{v_c} \quad (5)$$

A grid search is conducted over the three parameters (ϕ, i, v_c). For each set of tested parameters, the beamformed signal is computed as the sum of the time delayed traces divided by the total number of traces. The energy of the beamformed signal is estimated for each set of trial parameters, and the parameter set that yields the highest beamformed energy is kept as the most appropriate for the seismic event under consideration.

3.4 Quantitative assessment of DAS-derived acceleration

Recent studies explored the phase and amplitude response of DAS across various settings and frequencies, demonstrating the potential of DAS data for quantitative seismic applications (Lindsey *et al.* 2020; Paitz *et al.* 2021; Forbriger *et al.* 2025; Zhai *et al.* 2025). Evaluating DAS data relative to standard seismometer recordings remains important, as SR recordings can be influenced by installation specifics such as the intrinsic properties of the fiber optic cable – including fiber packing and outer coatings (Reinsch *et al.* 2017) – or its coupling methods (Willis *et al.* 2021; Forbriger *et al.* 2025). For a quantitative evaluation of the recorded phase and amplitudes, we use the goodness-of-fit (GOF) test introduced by Kristekova et al. (2006) to compare DAS and seismometer recordings. This test uses the continuous Morlet wavelet transform to calculate local envelope and phase differences over the signal of interest. GOF values range from zero (indicating no match) to 100 (indicating a perfect match). In addition

to the time-dependent GOF computed for phase and amplitude, a more compact representation of the fit is obtained for each trace using single-valued coefficients.

As illustrated in sixth row of Figure 2, acceleration traces derived from DAS across the vertical well are compared to the derivative of the vertical component of the 3C-broadband seismometer located at the wellhead (BUCH.HLZ trace). For the surface section, due to the variety of recording azimuths, we compare the DAS SR traces to the linear SR computed from the particle velocity recorded by the 3C-seismometer. This approach assumes that the recorded signals consist of single, non-dispersive plane waves with known incidence angles and phase velocities. We use the ray parameters evaluated according to Section 3.3 and the azimuths assigned to each DAS SP. For a given direction x of recording azimuth φ_x, Equation (6) gives the scaling relation between particle acceleration $a_x(t)$ and the linear SR $\dot{\varepsilon}_x(t)$ (see Appendix D for its derivation). s_h is the horizontal component of slowness and ϕ the back-azimuth, which are both estimated following Section 3.3.

$$\dot{\varepsilon}_x(t) = s_h \cdot \cos(\phi - \varphi_x - 180°) \cdot a_x(t) \quad (6)$$

4 Results

4.1 Signature of a M_L 0.5 seismic event

To illustrate the processing flow and assess the 3D- DAS array capabilities, we focus on the recording of a M_L 0.5 seismic event that occurred on January 15, 2023. Using the recordings of the local seismometer network (Figure 1a), this event was located in the zone of interest, close to the injection well of the geothermal plant of Pullach im Isartal, north-eastward from the seismic monitoring installation.

Figure 3 shows the waveforms of this event for all DAS SPs and for the collocated 3C-broadband seismometer. All traces are filtered between 5 and 50 Hz, after analysis of the time-frequency signal (see Appendix E). This event exhibits clear P- and S-wave arrivals, especially on the seismometer and borehole section of the DAS. The energy of the direct P-wave is mostly concentrated between 35 and 45 Hz. Although this higher frequency content reflects the proximity of the seismic source to Buchenhain, it implies that the resulting wavelength is short compared to the source-receiver distance of several kilometers, supporting the far-field assumption and approximation of incident plane wave.

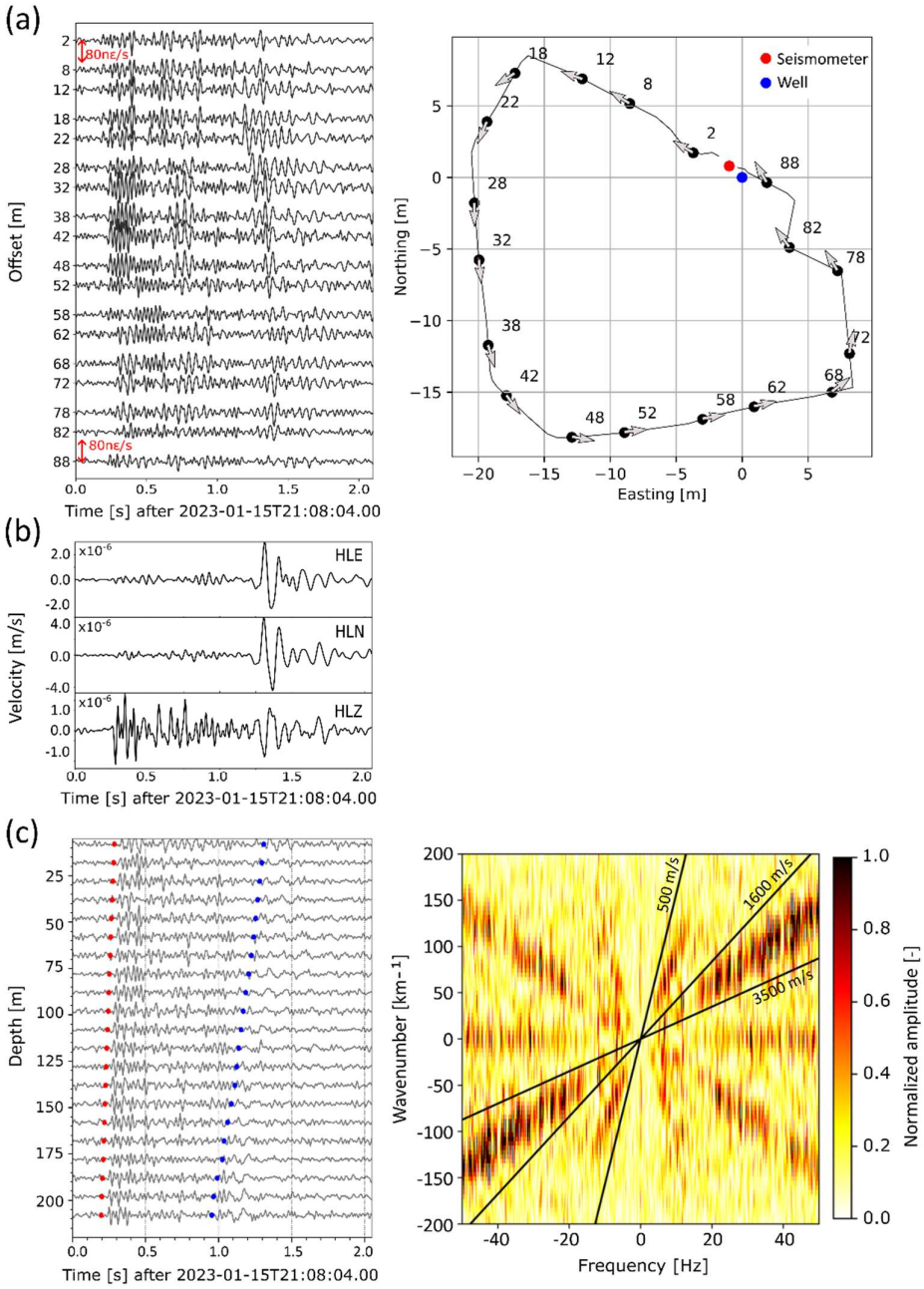

Figure 3: Waveforms of the 15 January 2023 seismic event. (a): SR recorded at the SPs along the two surface loops, after 5-50 Hz filtering, with the Y-axis indicating the offset from the start of the FOC loops. The red arrow represents an amplitude of 80 nε.s^{-1}. The location of the SP on the surface loop is shown in the right panel, with the label indicating the offset and the arrow the average azimuth computed over the gauge length. The reference for the

coordinate system is the location of the wellhead (blue dot). The red dot indicates the location of the seismometer. (b): Waveforms at the 3C-broadband seismometer BUCH after 5-50 Hz filtering. (c): in the left panel, SR recorded at the SPs along the vertical borehole after 5-50 Hz filtering and f-k filtering to isolate upward-propagating wavefronts. The picked P- (red points) and S- (blue points) wave onset times are shown. For the same time-period, the right panel presents the unfiltered in-well SR recordings in the f-k domain, with amplitude normalized to the maximum. The solid lines indicate the linear frequency-wavenumber relationships for three apparent velocities.

On Figure 3a, the DAS-traces of the surface loops are displayed according to their offset from the vault exit. The mapping of the corresponding SPs along the surface loops is shown in the right panel. The red arrow with a length of 80 $n\varepsilon.s^{-1}$ is representative of the maximum amplitude of the signal. This maximum amplitude exceeds the background SR noise usually recorded in this residential area (see Appendix F). Figure F1 highlights characteristic day–night and weekday–weekend background noise variations induced by the anthropogenic activity, with daytime SR levels typically reaching 30 $n\varepsilon{\cdot}s^{-1}$ and occasionally exceeding 50 $n\varepsilon{\cdot}s^{-1}$ during periods of increased presence in the park. The event under study occurred at 2023-01-15T21:08:03 (UTC), i.e., at night in local time (UTC+2) when anthropogenic seismic noise is reduced.

Figure 3b shows the 3C-seismogram of the broadband sensor, where the P- and S-waves are well differentiated in arrival times, frequency content and polarization. It is noticeable that the S-wave amplitude is larger than the P-wave.

Figure 3c focuses on the recordings from the vertical well, with the right panel showing the raw SR data in the f-k domain. The high amplitude along the horizontal axis (i.e., infinite apparent velocities) is characteristic of common-mode noise (Zhirnov et al., 2019). Apparent

positive and negative velocities ranging from 1600 to 3500 $m.s^{-1}$ and from 500 to 1600 $m.s^{-1}$ are observed too. They correspond respectively to P- and S-wavefields propagating either upward (positive frequency/positive wavenumber or negative frequency/negative wavenumber quadrants) or downward. In Figure 3c (left panel) the in-well SR traces are shown down to 210 m after band-pass filtering and applying a velocity filter configured to retain all up-going wavefields while removing common-mode noise. The three deepest traces, below 220 m, are excluded from the plot and further analyses because their proximity to the fiber termination leads to strong reflections, which degrade the signal quality. In addition, Appendix G shows the result of the narrow velocity filter targeting the P-wave and the S-wave separately. After applying the velocity filter, P- and S-wave onset times (marked in color in Figure 3c) are automatically picked according to the approach described in Section 3.2.

4.2 Signal to noise ratio and trace coherency

We examine how different filtering combinations impact signal coherence and SNR, focusing on the P-wave onset of the January 15 event. The SNR is computed from the RMS amplitudes in a 0.3-s signal window and a 3-s noise window, after and before the P-wave onset time respectively. Table 1 summarizes the resulting SNR, with all traces initially band-pass filtered between 5 and 50 Hz to target the event frequency range.

Table 1: SNR of the P-wave arrival of the January 15 event measured by DAS along the vertical (well) and horizontal (surface) sections of the FOC and by the 3C-seismometer (seismometer). All traces have been filtered between 5 and 50 Hz (BP, first row). For in-well DAS SPs, an additional velocity filter is considered to isolate either all up-going wavefields (f-k up-going) or only the up-going P-wavefield (f-k P-front) (second and third rows respectively). A trace summation after move-out correction was also applied (third row). In the fourth raw, a coherence-weighting is applied to the f-k filtered dataset to further

enhance the SNR. Average SNR values are given and, in parenthesis, the range over the multiple channels/SPs.

	DAS – well	DAS – surface	Seismometer
BP [5-50] Hz	3.6 (2.6 – 4.8)	3.7 (2.7 – 4.7)	8.2 (7.7 – 8.4)
BP + f-k (up-going)	5.7 (5.2 – 6.3)	n.a.	n.a.
BP + f-k (P-front)	6.8 (6.2 – 7.2)	n.a.	n.a.
BP + f-k (P-front) + stack	7.7	n.a.	n.a.
BP + f-k (P-front) + coherence enhancement	8.4 (8.0 – 8.5)	n.a.	n.a.

As observed, the 3C-seismometer has a SNR larger than the band-pass filtered DAS measurement, by a factor larger than two. For the DAS antenna in the well, different velocity filters are applied. The f-k filter, which keeps all up-going wavefields (positive frequency/positive wavenumber or negative frequency/negative wavenumber quadrants in Figure 3c-right), yields a 55% increase in average SNR compared to the sole band-pass filter (Table 1). Constraining the filter to keep the up-going P-wavefield only increases the SNR by a factor of almost two compared to the band-pass filter. After move-out correction and stack, the SNR in the well section further increases and reaches almost the 3C-seismometer level. This final 13% increase is larger than typically expected from stacking 21 traces, because the f-k filter has already substantially reduced random noise.

DAS data filtering also impacts the maximum correlation coefficients measured between pairs of SP. Figure 4 shows the correlation matrices of the SR traces recorded in the well (a) and on the surface (b) sections. The correlation was calculated on a 1.5 s window covering the P- and S-wavefronts, after 5-50 Hz band-pass filtering and, for the well section, the f-k filtering to keep the up-going P- and S-wavefields.

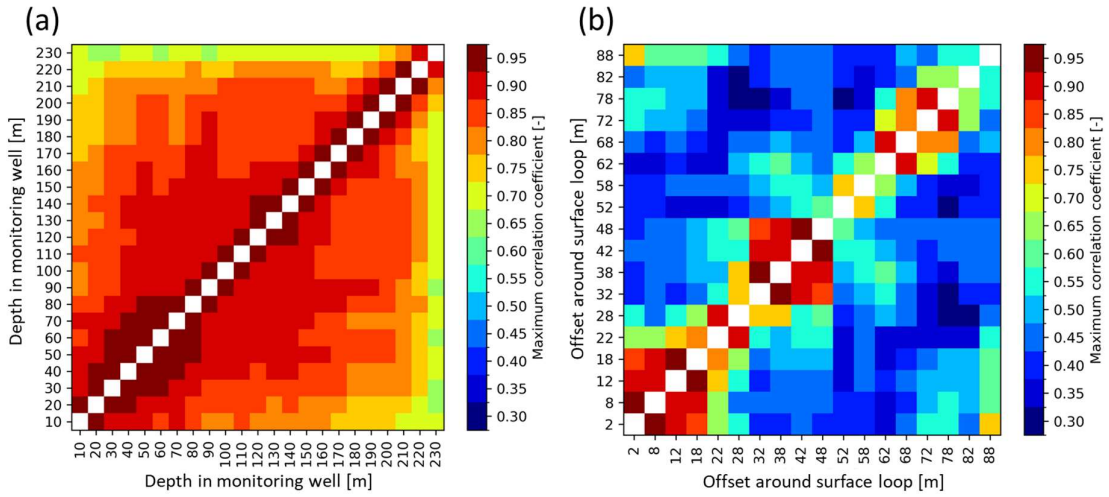

Figure 4: Maximum correlation coefficient between pairs of traces (a) along the vertical well, and (b) along the surface loop.

On the surface section, we observe significant correlation between SP measuring in similar (consecutive) azimuths (Figure 1). For instance, the maximum correlation coefficient, which exceeds 0.9, is observed with a combination of SR traces with offsets ranging from + 32 to + 48 m, along the almost north-south section of the loop. The maximum correlation coefficient measured between the traces oriented towards east, with offsets ranging from + 52 to + 62 m is lower with a maximum of 0.75. In the well section, the maximum correlation coefficients are above 0.7 for any combination of SP along the downhole cable.

4.3 Determination of seismic source parameters

Figure 5 illustrates the conversion of DAS SR to acceleration time-series for the January 15 event. Panel (a) displays all well traces, band-pass filtered between 5-50 Hz and f-k filtered to keep the up-going P- and S-wavefields as in Figure 3c, with the coherence window delineated by red lines. The conversion is carried out for the 120-m deep trace, which presents a strong first P-wave exceeding 70 nε.s^{-1} (Figure 5b). Figure 5c shows the coherence matrix computed with Equation (2), for apparent slowness ranging from -2.5 s.km^{-1} to -0.05 s.km^{-1}. We observe

clear variations associated with different phase arrivals in the slowness-time domain. The apparent slowness of the P-wave is well constrained, at -0.4 s.km^{-1} and the transition to S-wave slowness is evident in the coherence matrix. However, due to the lower frequency of the S-waves and as evidenced by the broader range of high coherence, the slowness estimate is less constrained compared to the P-waves. The computed slowness trace (red line in the coherence matrix) is then used in Equation (1) to convert SR to acceleration.

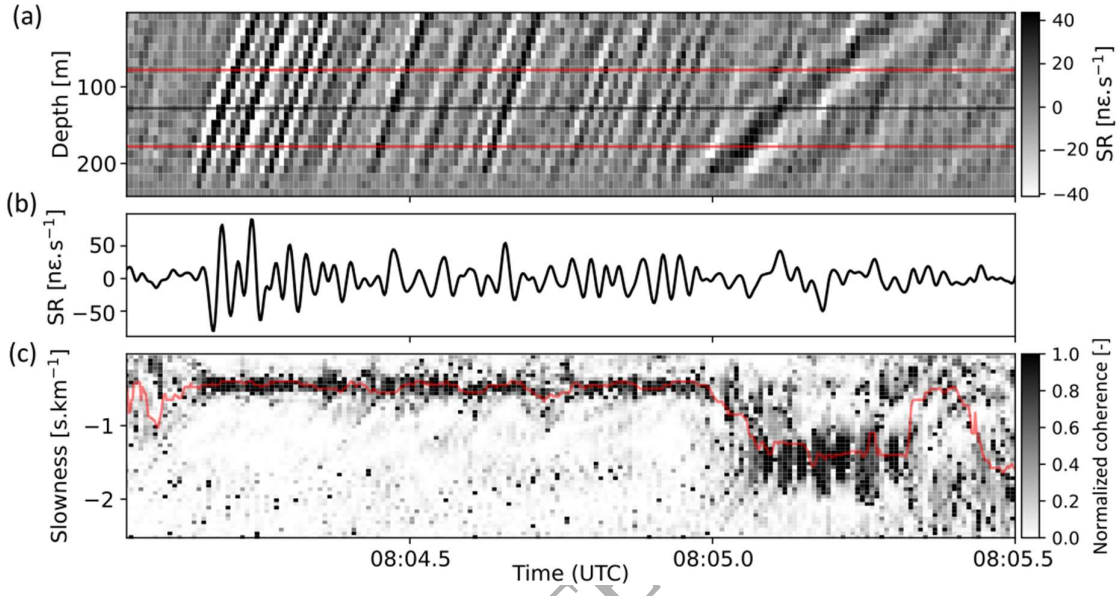

Figure 5: Determination of the slowness evolution for the January 15 seismic event. (a) shows the SR recorded in the well and the coherency window (solid red line) around the trace under consideration, here at 120 m. (b) displays the SR recorded at 120 m. (c) shows the coherence matrix, i.e. the time varying coherence values (gray scale) calculated for a range of slowness (vertical axis). The maximum coherence value (red line) indicates the slowness time-series used to convert SR to acceleration.

In parallel, this approach assigns each time-depth data point a coherence amplitude, which is then used for coherence-based weighting of the original SR data, as introduced by Schwarz (2019) and applied by Jousset et al. (2022). The resulting coherence-weighted

wavefield is presented in Appendix G. This approach further improves the SNR in DAS traces (Table 1), with the average value along the vertical antenna eventually exceeding that of the BUCH seismometer channels. Since this method does not preserve amplitude information, it is not suitable for source parameter estimation but remains useful for event detection or phase picking (Chen *et al.* 2023; Porras *et al.* 2024).

DAS-derived acceleration traces are used to estimate the seismic source parameters following the procedure outlined in Section 3.2. The same processing steps are applied to acceleration traces obtained after differentiating the recordings from the local seismological network. For the January 15 seismic event, we derive source parameters from the P-wave signal, due to clearer onsets and higher SNRs, and use 0.8-second-long windows starting at the P-wave onset time. The scalar moment M_0, the moment magnitude M_W, the corner frequency f_0 and the stress drop ΔS are estimated at each SP along the FOC. On the local seismological network, these parameters are estimated at every measurement site. Table 2 summarizes the average parameters obtained for each type of recording.

Table 2: Seismic source parameters of the January 15 event. DAS estimates are calculated for each SP in the well while the seismometer estimates are calculated at each monitoring site of the local seismometer network (see Figure 1).The table gives the average scalar moment M_0 (N.m), moment magnitude M_W, corner frequency f_0 (Hz), stress drop ΔS (Pa) and low-frequency displacement amplitude plateau Ω_0 ($m.s^{-2}.Hz^{-1}$).

	M_0 [N.m]	M_W [-]	f_0 [Hz]	ΔS [Pa]	Ω_0 [$m.s^{-2}.Hz^{-1}$]
DAS	6.50×10^9	0.47	45	8.95×10^5	8.90×10^{-10}
Seismometer network	6.60×10^9	0.48	49	1.30×10^6	9.25×10^{-10}

In addition, Figure 6 shows the distribution of the DAS-estimates to the ratio of the average value obtained on the seismometer network.

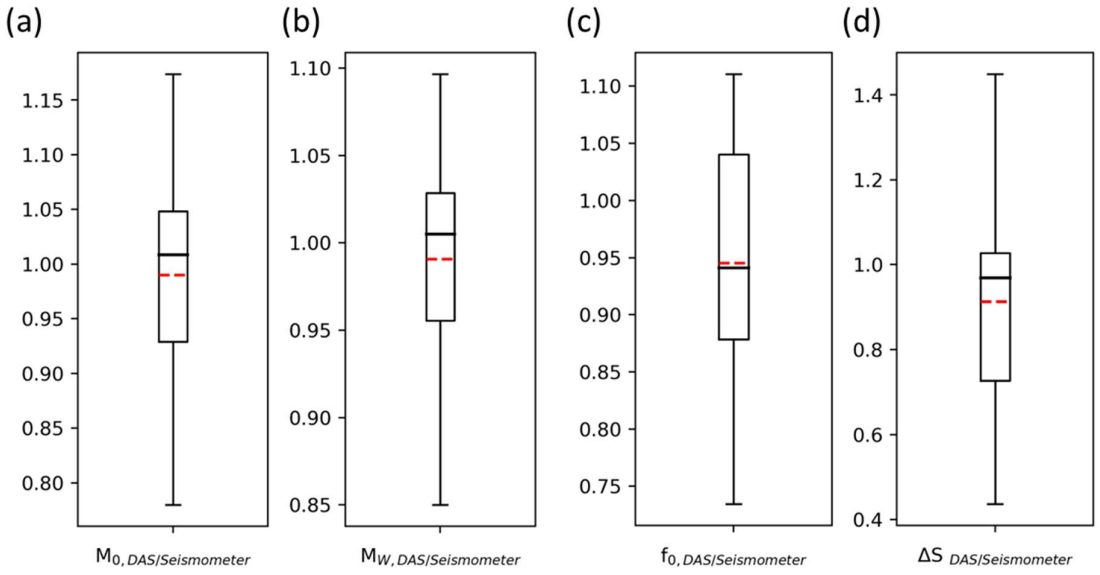

Figure 6: For the January 15 seismic event, distribution of the ratio between the source parameters estimated at each DAS SPs along the well section with the average calculated on the local seismometer network. (a), (b), (c) and (d) show the ratios of the scalar seismic moment, moment magnitude, corner frequency and stress-drop respectively. Each boxplot includes the average ratio in red, the median ratio in black, the box delimits the first and third quartiles and the whiskers extend from minimum to maximum ratio.

DAS-based M_0 estimates (Figure 6a) are in good agreement with the reference value, as indicated by an average ratio of 0.98. The relatively small spread of values among DAS SPs reflects consistent measurements along the vertical FOC. Consequently, the moment magnitude estimated from DAS is also reliable. A ratio of 0.95 is observed for the corner frequency. Since stress drop depends on the seismic moment and on the cube of the corner frequency (Equation (4)), this parameter exhibits the largest spread in differences between estimates from DAS and seismometer recordings. The average ratio is 0.91.

4.4 Ray parameters from DAS

Using the surface and vertical recordings from the 3D-DAS array, the incidence and back azimuth of the February 15 seismic event can be determined. We focus on the higher frequency P-wave signal, as the compact layout of the DAS array limits the resolution of lower-frequency phases, which is further analyzed in Sections 4.7 and 5.1. Inter-channel time-delays are calculated using Equation (5) and applied to the band-pass filtered traces from the surface loop and to the band-pass and f-k filtered traces from the well section before beamforming. The beam energy is computed on successive overlapping 0.3-second windows, which corresponds to approximately 10 times the main period of the P-wave signal under consideration. The results of the analysis are illustrated by two radar plots in Figure 7. Panel (a) shows the back azimuth and the horizontal apparent velocity that focuses the signal energy on the horizontal plane. As observed, the spread of the P-wave back azimuths is low among the tested bins, which underlines the consistency of DAS-estimates. In Figure 7b, the beam incidence is evaluated in the vertical plane oriented according to the estimated back azimuth. The incidence and vertical slowness are displayed as in Figure 7a, showing a similar clustering of the beam energy.

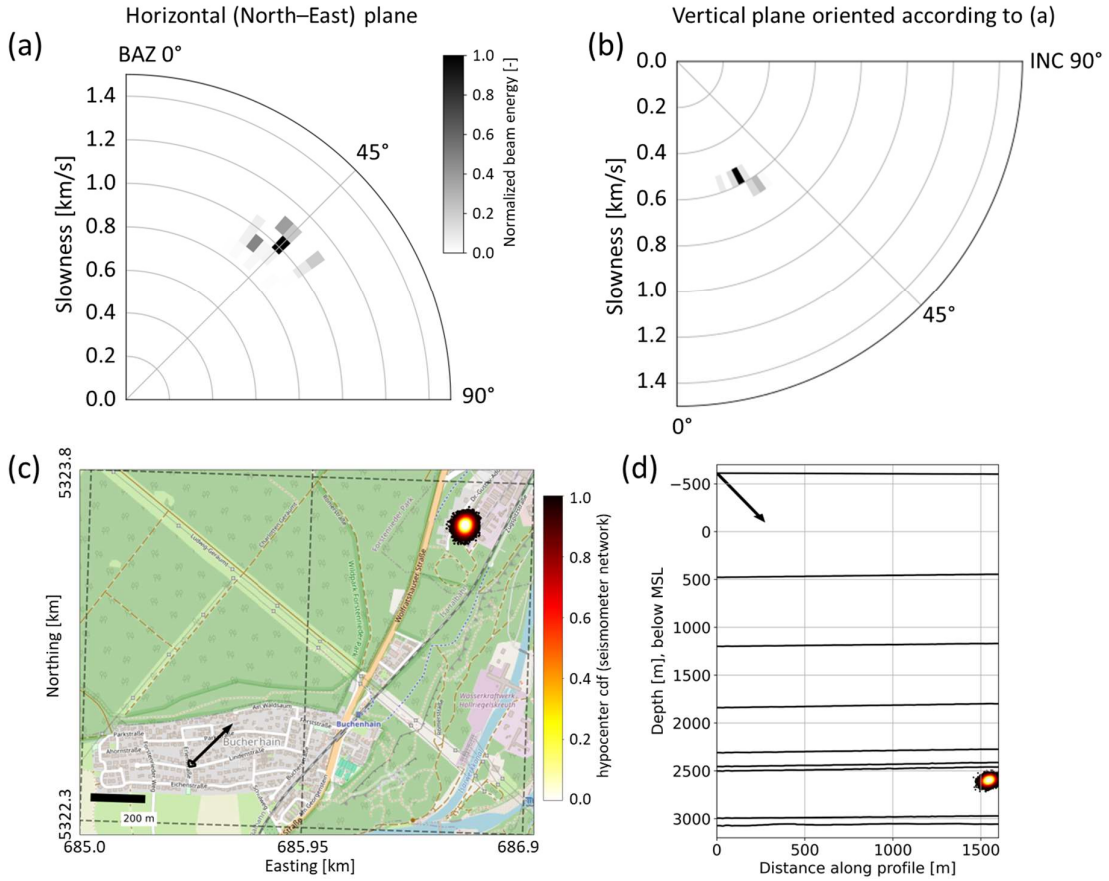

Figure 7: For the January 15 seismic event, ray parameters obtained using borehole and surface DAS data. (a): polar plot of the normalized beam energy as a function of the back azimuth (angle) and beam slowness (radius) for the corresponding bin. (b): same as (a) in the vertical plane oriented along the back-azimuth determined in (a), where the angle from the vertical indicates the event incidence angle. (c): map including the most likely back azimuth computed from DAS recordings (black arrow) and surface projection of the cumulative distribution function (cdf) of the event hypocenter derived from the seismometer network (light colors). The cdf is color-coded and clipped at 68% confidence interval. (d): in the vertical plane crossing the DAS well and the event hypocenter (as calculated by the seismometer network), most likely incidence angle measured from DAS (black arrow), layer interfaces from the 3D velocity model (black lines) and projection of the cdf derived from the seismometer network.

We compare DAS-derived ray parameters and the hypocenter estimated from the seismometer network (see fifth row in Figure 2). The latter was obtained using NonLinLoc (Lomax *et al.* 2000, 2014) and a 3D velocity model of the study area (Azzola and Gaucher 2024). Hypocenter determination uses a weighted least-square minimization of the arrival time residuals with an Oct-Tree grid-search (Lomax and Curtis 2001) and importance sampling provides probability density functions to estimate location uncertainties. The cumulative distribution function around the most likely hypocenter is projected on a map (Figure 7c) and in a vertical plane (Figure 7d) up to the 68% confidence level. The ray parameters derived from DAS recordings are represented as an arrow pointing in direction of back-azimuth (Figure 7c) and incidence (Figure 7d). Table 3 gives the values of the back-azimuth and incidence angles obtained in both cases, where uncertainties on the beam parameters from the seismometer network are computed from the spatial extent of the 68% confidence level shown in Figure 7. At the BUCH 3C-broadband seismometer, polarization analysis of the P-wave onset (fourth row in Figure 2) is carried out to obtain the back azimuth and incidence of the wave as proposed by Flinn (1965). This single seismometer approach computes the principal eigenvector of the three-component covariance matrix around the P-wave arrival, which indicates the P-wave propagation direction.

Table 3: Ray parameters of the January 15 seismic event measured at the Buchenhain monitoring installation, including back azimuth (BAZ), incidence (INC) and corresponding horizontal and vertical apparent velocities.

Beam parameters	**BAZ [°]**	**INC [°]**	**($v_{app,\,h}$, $v_{app,\,z}$), P-wave [m.s-1]**
From DAS	43	29	(945, 1705)
From NonLinLoc hypocenter	44 ± 1.5	29 ± 2.1	n.a.
From BUCH.HL*	41	18	n.a.

These measurements show that the DAS-estimates are within the confidence interval of the NonLinLoc location. In contrast, the ray parameters computed from the single BUCH seismometer do not agree with those from the seismometer network or from DAS (see Section 5.2).

4.5 Recorded phase and amplitude

In this study, the FOC was cemented behind the casing or tightly packed in a trench, and we used tight-buffered single-mode fibers, which describes favorable conditions to the acquisition of high-quality DAS data (e.g., Willis *et al.* 2021). The relative consistency between DAS- and seismometer-estimates in sections 4.3 and 4.4 suggests that DAS-based acceleration traces are representative of ground motion across the studied frequency range. For quantitative analysis, we use the GOF test described in Section 3.4.

In the vertical well, we compare the DAS recordings with data from vertical channel of the seismometer installed in the vault, next to the wellhead, as described in Section 3.4. Figure 8a shows the evolution of the GOF coefficients of the phase and amplitude over the well section.

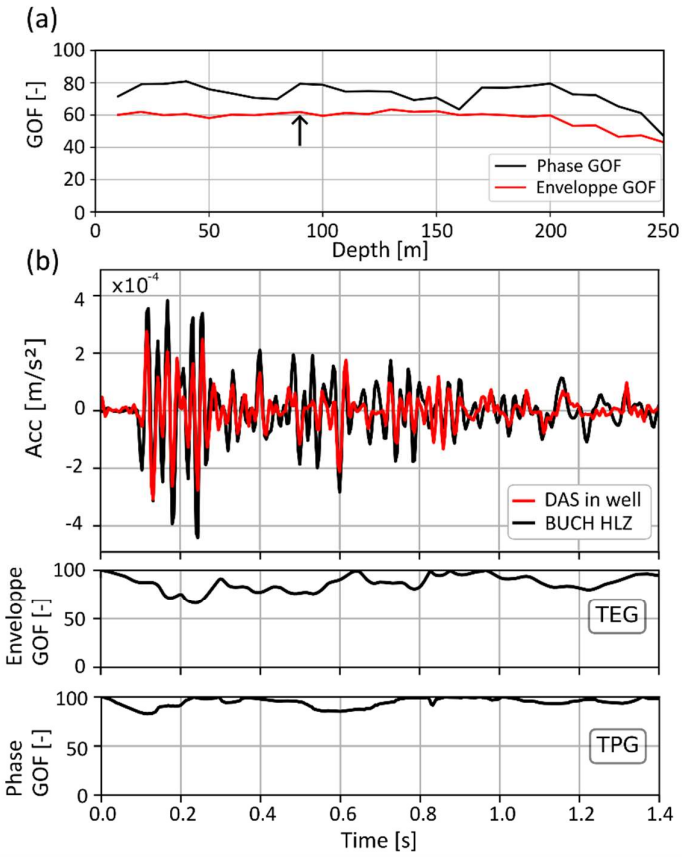

Figure 8: January 15 seismic event. (a): GOF coefficient for the envelope (red) and phase (black) as a function of depth in the well. The arrow shows the DAS SP that is further analyzed using the comprehensive time- GOF analysis in panel (b). (b): GOF between the 90-m-deep DAS trace and the seismometer trace. The top row compares the BUCH HLZ and DAS waveforms after conversion to acceleration. The middle and bottom rows show the normalized goodness-of-fit (GOF) of the waveform envelope (TEG) and phase (TPG) in the time domain, respectively.

The phase of the DAS-derived acceleration waveforms is consistent with the phase of the seismometer acceleration derived from the vertical channel, as indicated by the average phase-GOF values, which are predominantly above 60%. This consistency also extends to the

envelope, with values close to 60% across the vertical well. A decrease in GOF coefficients is observed notably below 220 m in the well. This may be due to disturbances associated with the proximity of the cable termination but also to heterogeneity of the propagation medium. These traces were nevertheless excluded from the previous analysis of source parameters.

Figure 8b details the results, in the time and frequency domains, for the DAS SP at 90 m below ground level, for which the highest amplitude GOF is observed in panel (a). The agreement is evident both temporally and across frequencies. The figure shows that the DAS (red curve) captures the correct P-wave arrival time and polarity seen at the BUCH seismometer (black curve). Although a larger discrepancy of the direct S-wave is observed (after 1.1 s in Figure 8b), the first arrival is still consistently detected, albeit less distinctly. The signal amplitudes fit relatively well, despite the sensors not being co-located.

We applied the same GOF test on the recordings of the surface loop after converting the seismometer recordings as described in Section 3.4. Figure 9a summarizes the results of the analysis and shows that the phase and envelope of the DAS and seismometer SR are less consistent for the surface loop than for the well section. Most of the GOF coefficients are above 50%, except for specific SPs where they are significantly below, for example at +8 m and +42 m (+2 m and +78 m to a lower extent). The effect is particularly pronounced on the GOF envelope.

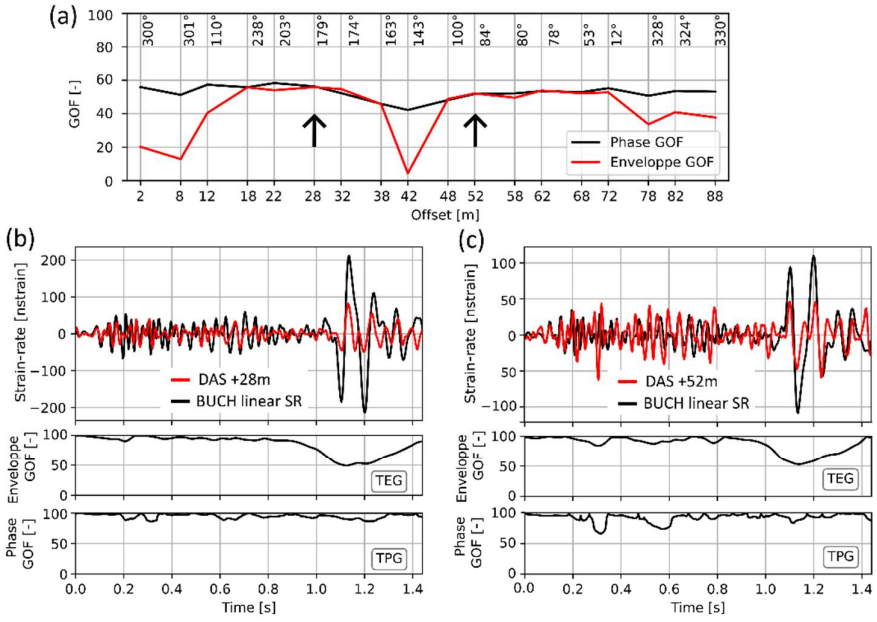

Figure 9: January 15 seismic event. (a): GOF coefficient for the envelope (red) and phase (black) as a function of the offset along the surface loop. The arrow indicates the two DAS SPs for which comprehensive time-frequency goodness-of-fit analysis is made (panel (b) and (c)). The upper labels indicate the recording azimuth of each SP quantified by the average orientation of the cable over the gauge length. (b) and (c) focus on DAS SPs with orientation close to N180°E (offset 28 m) and N90°E (offset 52 m), respectively. In both panels, the top row compares the SR waveform computed from BUCH channels with the DAS SR waveform. The middle and bottom rows show the normalized goodness-of-fit (GOF) of the waveform envelope (TEG) and phase (TPG) in the time domain, respectively.

Considering Equation (6), used to convert the seismometer recordings, the strain-rate amplitude is expected to decrease as the back-azimuth becomes perpendicular to the recording azimuth. For the January 15 event, this occur at φ_x= 315° or φ_x= 135°, that is at the vicinity of the SPs with offset +8 m and +42 m (see Figure 1). Under such circumstances, the

linear SR computed from particle velocity is primarily influenced by non-plane wave contributions. Hence, the comparison between seismometer and DAS SR signals fails at these SPs, as illustrated in Figure 9a at + 8m and +42 m. The variability observed in the GOF coefficients may also arise from assumptions regarding the recording azimuth of the DAS SP, as deviations of the fiber from a straight path along the corresponding GL introduce a certain degree of uncertainty in the phase summation. However, according to the theoretical framework proposed by Näsholm et al. (2022), verifying the findings of Bowden et al. (2021), the cable orientation variations along the GL can be compensated if the radius of curvature is sufficiently large (or the curvature is sufficiently small) relative to the seismic signal wavelength. According to Figure 9a, this could explain relatively high GOF coefficients at an offset of +48 m, where the average recording azimuth over the gauge length is approximately eastward, and the SP itself is situated at a bend in the cable trajectory.

Figure 9 finally presents the time-dependent GOF test for recording azimuths nearly oriented towards North (panel (b)) and East (panel (c)). For the P wave front, both subplots show that the phase is well adjusted, and that the first motion and its amplitude are consistent between both measurements. The discrepancies in later P-phases may be attributed to the limitations of the plane wave assumption. Figure 9 shows a more variable adjustment over the S-phase, for which DAS SR is, for example, weaker compared to linear SR obtained from particle velocity. This adjustment of the S-phases also impairs the integrated GOF coefficients presented in Figure 9a.

4.6 Results on an extended seismic catalog

The seismometer network monitoring the area (Figure 1) can detect seismic events with a moment magnitude down to -0.8 around Pullach (Azzola et al. 2021), which is the targeted monitoring area for the DAS array. During the recording period of the DAS array, only the

January 15 event occurred in this zone. Consequently, a statistical assessment of the accuracy of the DAS estimates cannot be carried out. However, 29 seismic events located outside the zone of interest were observed during that period. These events are grouped into two clusters, located approximately 5 km and 12 km east of the Buchenhain monitoring installation (Figure 1). For this extended catalogue, we analyze differences in seismic source parameters derived from DAS and the conventional seismometer network (Figure 10) in relation to key features of each event, including the distance from the DAS array to the epicenter, the average SNR on the surface loop SPs, and the signal frequency content.

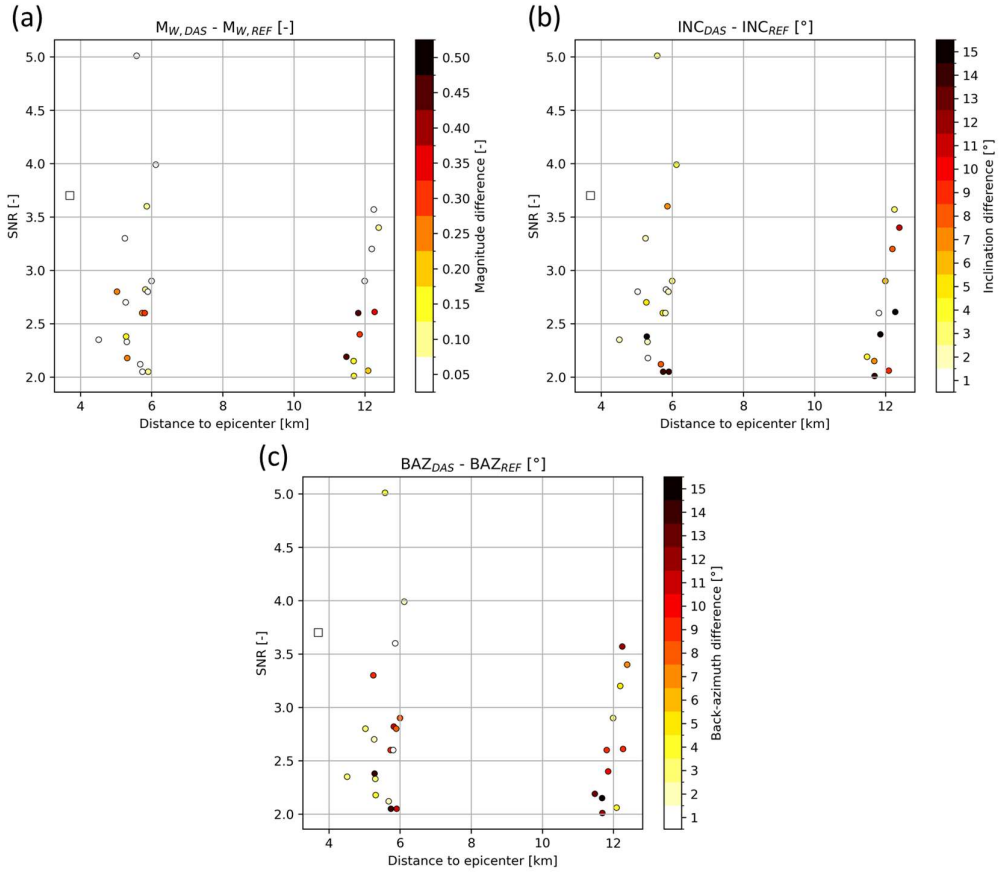

Figure 10: For the 29 events recorded outside the seismic network, difference between moment magnitudes (a), incidences (b) and back azimuths (c) calculated using the DAS recordings and using the seismometer network (with index REF). The color scale gives the differences between the values. The differences are shown in function of the distance to the

epicenters (horizontal axis) and to the SNR (vertical axis). The displayed SNR is the average value computed over DAS SPs from the surface loop and measured after application of the 5-50 Hz band-pass filter. The square marker indicates the January 15 event.

The moment magnitudes and P-wave incidence angles derived from the vertical DAS antenna are mostly consistent with those obtained by the seismometer network, as illustrated by Figure 10a and Figure 10b. The median difference in moment magnitude is 0.11 and ranges up to 0.5. The median difference in incidence angle is 4.5° and ranges up to 15°. In contrast, discrepancies in back-azimuth are more significant with a median value of 7.5°.

4.7 3D-DAS array response

We estimate the sensitivity and resolution of the 3D-DAS array by computing the array response in three dimensions. The theory of array response is well-documented for seismic arrays composed of 3C-seismometers (Haubrich, 1968; Iyer, 1968; Mykkeltveit et al., 1983; Johnson and Dudgeon, 1993). In the case of the 3D-DAS array, we first consider that a seismometer is virtually placed at the position of each SP, without accounting for effects related to the directionality of the incoming wave field or the orientation of the GLs. Figure 11 shows the distribution of beam energy on slices extracted in different planes: (s_X, s_Y) in panel (a) and (s_X, s_Z) in panel (b). To investigate frequency-dependent effects (and thus differences related to epicentral distance), we also vary the frequency range, from panel (a), which considers frequencies typical of the January 15 seismic event, to panel (c), which is representative of the extended catalogue.

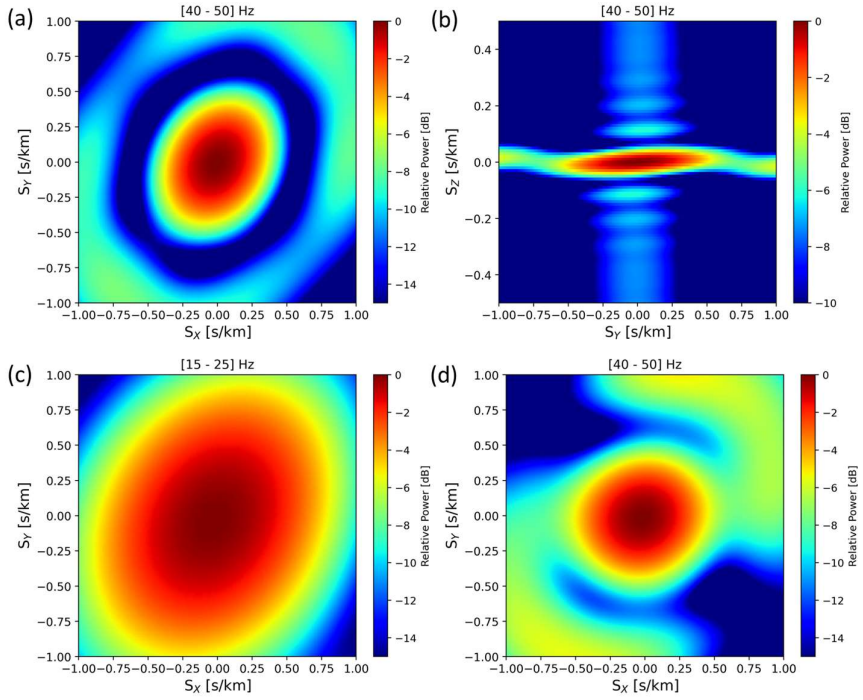

Figure 11: Relative power of the array response (in dB), normalized to its maximum, as a function of slowness differences within a specified frequency range, as indicated in titles. Array responses are calculated for incremental frequencies within the queried range and then averaged. The responses are calculated in 3D for the full DAS array and slices are extracted for visualization. (a) displays the response in the (s_X, s_Y) plane with s_Z = 0, panel (b) shows the response in the (s_X, s_Z) plane with s_Y = 0. Panel (c) focuses on a lower frequency range compared to panel (a). In panels (a), (b) and (c), the calculation assumes that a seismometer is positioned at each DAS SP. In (d), the orientation of the SPs and the wave field directionality are accounted for, focusing on the (s_X, s_Y) plane, the BAZ of the January 15, 2023 seismic event and its characteristic frequency range (40 to 50 Hz).

To account for the orientation of the FOC and the directionality of the wave field, we applied the methodology proposed by Kennett (2022), which modulates the beam energy by a generic response determined by the array geometry. Applied to the P-wave signal of the January 15 seismic event under study, the array response in the s_X–s_Y plane is shown in Figure 11d.

5 Discussion

5.1 Interpretation of the 3D-DAS array response

As illustrated in Figure 10 with the processing of the seismic events located outside the zone of interest (see Section 4.5), discrepancies between the ray parameters estimated from the 3D-DAS array processing and their expected values increase with event distance and with decreasing SNR. A lower SNR that would impair trace coherence and thus limit DAS beamforming has already been outlined in the literature (van den Ende and Ampuero 2021; Muñoz and Soto 2022; Lentas *et al.* 2023). To further investigate these differences as a function of epicentral distance — and thus signal frequency —the distribution of the beam energy in the 3D-DAS array response, as presented in Section 4.7 and Figure 11, should be further analyzed.

The spatial arrangement of sensors determines the azimuthal sensitivity of the array. For the DAS array surface loop, we observe a spherical main lobe indicating a good azimuthal resolution with limited orientation effects (Figure 11a and Figure 11c), remembering that the FOC directionality is not accounted for in this analysis. The resolution to smaller wavenumbers is influenced by the aperture, with the longest resolvable wavelength being roughly the same as the aperture. The aperture of the surface loop is 32 m, resulting in a relatively broad main lobe, as shown in Figure 11a. This limits the array capacity to resolve apparent velocities in the horizontal plane, which is even stronger for low frequency signals (Figure 11c). These resolution limitations are mitigated for the January 15 event, with signals primarily visible around 40 Hz. On the other hand, seismic signals from the extended catalog are more subject to attenuation effects due to the greater distance to the hypocenter. They are characterized by lower-frequency content, with energy mostly concentrated around 20 Hz. In the vertical plane (Figure 11b), the main lobe is considerably narrower because of the larger aperture of

the vertical well, which results in a higher resolution in measuring vertical apparent velocities. The higher sensitivity and resolution to incident wavefield and vertical apparent velocities likely explain the smaller median difference in incidence, compared to the back azimuth (see Figure 10).

Similarly, sensors spacing determines the smallest resolvable wavelength, which is reflected in the location of the side lobes in the array response. In our setup, the spacing in the vertical well is imposed by the acquisition parameters (10 m spatial sampling), whereas a shorter inter-channel spacing is achieved along the surface loop through the cable geometry and the double-loop configuration. These short distances are an advantage of the DAS array, improving its resolution for the shorter wavelengths targeted in this study.

When considering that the beam energy is modulated by a generic response determined by the array geometry (Figure 11d), we observe that the array response remains well-focused with directional effects amplifying the side lobes, particularly along the Northeast–Southwest axis. In addition, Figure H2 (in Appendix H) illustrates the directional effects on the array response shown in Figure 11c, assuming an incoming wavefield with an azimuth of N80°E, which is representative of the barycenter of the two seismic clusters located east of the Buchenhain monitoring installation. The features observed in these array responses confirm the sensitivity and resolution characteristics inferred for the array of DAS SPs based on the analysis of panels (a) and (c) of Figure 11.

This analysis underlines that the geometry of the 3D-DAS array provides a good azimuthal response due to the loop configuration and a valuable array response for P-waves from the local monitoring zone. It also emphasizes the limitations of the DAS array in resolving the back-azimuth of seismic events originating from outside the target monitoring area. In view of

Figure 11, similar limitations would also apply to an array of sensors without the directional sensitivity constraints associated with DAS SPs.

5.2 Potential for transferability and standardization in monitoring workflows

In future deployments, the design of the FOC surface loop should be motivated by the monitoring objectives and the expected signal wavelengths. The latter guides the selection of the GL and, in turn, the required minimum length of straight cable segments. The maximum resolvable wavelength is approximately equal to the array aperture. Smaller wavelengths can be analyzed with finer precision provided that the DAS channel spacing meets the spatial Nyquist criterion. However, in practice, the geometry of such urban monitoring installation is constrained by the available space, which limits the achievable surface aperture. Alternatively, the surface array could be extended using existing near-surface telecommunication fibers, though this would introduce additional challenges, particularly in quantifying and ensuring adequate coupling between the fiber-optic cable and the ground (e.g., Yang Li *et al.*, 2023). The minimum required well depth is controlled by the SP spacing and GL, as the proposed conversion from SR to acceleration requires a sufficient number of spatially coherent yet independent traces to contribute to the coherence window (see Section 3.2). The concept of a self-contained 3D-DAS array could also be applied to repurpose abandoned oil and gas wells, providing an environmentally responsible and technically valuable approach to extend the lifetime of existing subsurface assets (Sidenko *et al.* 2022; Lellouch and Wetzler 2025).

As shown by the results (Section 4), unconventional seismic instrumentation based on DAS can support passive monitoring of local seismicity, even in complex urban environments. The comparison of source parameters obtained from DAS and seismometers (Figure 6) showed that converted DAS SR data provide reliable and homogeneous magnitude estimates. The

large number of SP along the FOC enhances the statistical robustness of the determination of the source parameters, however, from a single antenna. In contrast, the local seismometer network provides fewer observations from different sites, but with site effects that may vary. Moreover, the vertical alignment of the SPs in the well supports the analysis of highly coherent, well-resolved wavefields (Figure 4), a feature that could also be exploited to increase the sensitivity in detecting seismic events (Lellouch et al. 2019).

Beyond the source parameters extracted from in-well DAS recordings, beamforming on the 3D-DAS array for the January 15 event provided back-azimuth and incidence angle estimates that agree with the hypocenter location independently computed from the conventional seismometer network (Figure 7). Furthermore, as shown with the extended event catalog (Figure 10), the DAS array can provide additional constraints that contribute to improved hypocenter depth estimation. In contrast, the ray parameters computed from the single BUCH 3C-seismometer are inconsistent with those derived from either the DAS array or the seismometer network (Table 3). In particular, the differences observed in the incidence angles may come from the measurement approaches: a single-point evaluation at the surface compared to a calculation integrating measurements over a 210-m vertical section. Shallow velocity variations near the surface could bend the seismic ray, resulting in an incidence angle closer to vertical at the seismometer. Besides, DAS data processing assumes that a dominating incident plane wave is reaching the vertical antenna.

From an instrumentation perspective, the 3D-DAS array can, to some extent, be compared to a (mini-)array of geophones, with the advantage of a higher spatial density, albeit without the three-component sensitivity of individual geophones. The dense sampling and continuous coverage along the fiber allow for coherent array processing over extended distances. From a cost perspective, the IU represents the primary investment, whereas fiber-optic cables

themselves are much cheaper. This IU can yet be redeployed across sites or used to operate multiple DAS arrays if suitable fiber connections exist. However, achieving a comparable spatial resolution with conventional geophones involves significant investment in instrumentation. Beyond the local seismic monitoring of geothermal developments in southern Munich, such a 3D-DAS array would be also relevant for local monitoring of other geo-energy infrastructures such as Mining, Underground Thermal Energy Storage (UTES) or carbon capture and sequestration (CCS) projects.

On the long-term, the integration of comparable DAS installations into (inter-)national monitoring infrastructures will require progress toward the standardization of data types, (meta)data formats, transfer protocols, and processing methods likely mixing seismological, seismics and array processing workflow. The presented conversion and event characterization procedures contribute to standardization efforts, and the phase and amplitude comparison suggest that DAS and seismometer recordings could be merged for quantitative seismic monitoring (see Section 4.5). This integration presents computational challenges too. The conversion procedure from SR to acceleration is computationally intensive because it involves maximizing coherence over slowness, time, and space, which currently limits its suitability for near-real-time use (e.g., Azzola and Gaucher 2024). Also, the dataflow produced by the 3D-DAS array of about 1.8 GB per hour corresponds to roughly 15.7 TB per year. If storing these data volumes is feasible, streaming the full dataset over a mobile network is still not realistic. However, an upgrade in future implementations could be to stream selected DAS traces via standard seismological protocols (Bâ *et al.* 2025; Morten *et al.* 2025) to enable their integration into automatic seismic monitoring workflows.

6 Conclusions

This study describes the implementation of an experimental seismic monitoring installation equipped with a three-dimensional DAS array for monitoring seismic activity associated with local deep geothermal fields, in the southern Munich region. By using DAS along a fiber-optic cable deployed horizontally near the surface and vertically in a monitoring well, the setup enables three-dimensional analysis of the incoming wavefields. The capabilities of the processing workflow are demonstrated with a $M_W = 0.48$ nearby seismic event. It is then generalized to seismicity that was located up to 15-km away. The study highlights the ability of the 3D-DAS array to resolve ray parameters, i.e. back azimuth, incidence angle and slowness vector, thanks to a time-domain 3D beamforming algorithm. In addition, it is shown that the vertical well section can advantageously be used to convert the DAS SR data to ground acceleration using adaptive slowness estimation. This data-driven conversion facilitates the estimation of seismic source parameters using established processing methods, which supports the integration of DAS into more standard seismic monitoring practices.

The comparison of the DAS-derived ray parameters, seismic moments, moment magnitudes, and stress drops with those obtained by the local seismometer network confirms the proposed methodology and the robustness of the DAS-derived results. As an additional validation step, we compare recordings from the collocated 3C broadband seismometer of the local network with waveforms from both the near-surface and downhole fiber sections using phase- and amplitude-based goodness-of-fit metrics. The results support the reliability of the ground motion estimates obtained from DAS data and underline the potential of DAS as a complementary tool for estimating wavefield properties.

The analysis of the resolution and sensitivity of the 3D-DAS-array evidences the reduced resolution and SNR of the DAS along the surface section, which limits the effectiveness of the

seismic source parameter estimation for distant or low frequency events. This limitation arises from the compact geometry of the surface loop, shorter than 100-m, which constrains azimuthal resolution and reduces its sensitivity to low wavenumbers. However, any other standard array of seismometers with a comparable layout would face similar constraints. The array response analysis confirms that the spatial density and surface geometry of the DAS array provides adequate resolution and directional coverage for seismic monitoring in a radius of 4 km.

From another perspective, the geometry of the 3D-DAS array could be used in future research to extract subsurface elastic properties from ambient seismic noise by correlating borehole and surface recordings. If successful, this approach could extend the monitoring capabilities of the 3D-DAS array to continuous monitoring of subsurface changes.

Data and resources

The DAS strain-rate (SR) dataset from the January 15, 2023 seismic event and a Python script used for loading, visualizing, and processing the DAS data, is publicly available at the following DOI: 10.35097/j8zkf8fnb0uh5q88. DAS strain-rate recordings acquired during other time periods are available from the corresponding author upon request.

Funding

This work was conducted in the frame of the INSIDE project (https://inside-geothermie.de/en/inside-en/), which was supported by the German Federal Ministry for Economic Affairs and Climate Action and the Project Management Jülich (PtJ) under the grant agreement number 03EE4008C.

Declaration of Competing Interests

The authors declare no competing interests.

Acknowledgments

We would like to thank all members of the INSIDE project, Innovative Energie für Pullach GmbH and Stadtwerke München GmbH, for their fruitful contributions to the project. We express particular thanks to Innovative Energie Pullach (IEP) GmbH for their contribution to the design and implementation of the seismic monitoring installation. We thank the FEBUS Optics company for their continuous logistical support associated with the DAS equipment. Finally, we are grateful to our colleagues from the Geophysical Institute of KIT (GPI), Felix Bögelspacher, Michael Frietsch and Andreas Rietbrock who helped to implement and maintain the surface seismic monitoring network.

Author Contributions

A.J.: Conceptualization (Equal), Formal analysis (Lead), Investigation (Lead), Methodology (Lead), Project administration (Supporting), Software (Lead), Supervision (Lead), Visualization (Lead), Writing - original draft (Lead), Writing - review & editing (Equal).

G.E.: Conceptualization (Equal), Investigation (Supporting), Methodology (Supporting), Project administration (Lead), Writing - review & editing (Equal)

References

Anderson, J.G. & Hough, S.E., 1984. A model for the shape of the fourier amplitude spectrum of acceleration at high frequencies. *Bulletin of the Seismological Society of America*, **74**, 1969–1993. doi:10.1785/BSSA0740051969

Azzola, J. & Gaucher, E., 2024. Seismic Monitoring of a Deep Geothermal Field in Munich (Germany) Using Borehole Distributed Acoustic Sensing. *Sensors*, **24**, 3061. doi:10.3390/s24103061

Azzola, J., Thiemann, K. & Gaucher, E., 2023. Integration of distributed acoustic sensing for real-time seismic monitoring of a geothermal field. *Geotherm Energy*, **11**, 30. doi:10.1186/s40517-023-00272-4

Bâ, D.N., Pellicer, R. sánchez-, Huynh, C., Hibert, C., Malet, J., Calbris, G. & Duret, F., 2025. Fiber-Optic Monitoring of Onshore Pipelines: Applications in Third Party Detection and Seismic Monitoring, Vol. 2025, pp. 1–5, Presented at the 86th EAGE Annual Conference & Exhibition, European Association of Geoscientists & Engineers. doi:10.3997/2214-4609.2025101186

Beyreuther, M., Barsch, R., Krischer, L., Megies, T., Behr, Y. & Wassermann, J., 2010. ObsPy: A Python Toolbox for Seismology. *Seismological Research Letters*, **81**, 530–533. doi:10.1785/gssrl.81.3.530

Bowden, D.C., Klaasen, S., Martin, E., Paitz, P. & Fichtner, A., 2021, March 4. Wave-selective beamforming with Distributed Acoustic Sensing. doi:10.5194/egusphere-egu21-12216

Bundesverband Geothermie, 2024, June. Nutzung der Tiefen Geothermie in Deutschland, Poster presentation, . Retrieved from https://www.geothermie.de/fileadmin/user_upload/Aktuelles/Geothermie_in_Zahlen/BVG_Poster_Tiefe_Geothermie_2024_web.pdf

Butterworth, S., 1930. On the Theory of Filter Amplifiers. *Experimental Wireless and the Wireless Engineer*, **7**, 536–541.

Chen, Y., Savvaidis, A., Chen, Y., Saad, O.M. & Fomel, S., 2023. Enhancing earthquake detection from distributed acoustic sensing data by coherency measure and moving-rank-reduction filtering. *GEOPHYSICS*, **88**, WC13–WC23. doi:10.1190/geo2023-0020.1

Cröniger, C., Tretter, R., Eichenseer, P., Kleinertz, B., Timpe, C., Bürger, V. & Cludius, J., 2022. *Approach to Climate Neutral Heat Supply in Munich 2035*, Oral presentation, .

Dakin, J.P., 1990. Distributed optical fibre sensors, Presented at the OFS-7: Conference on Optical Fiber Sensors (02/12/90 - 06/12/90). Retrieved from https://eprints.soton.ac.uk/77464/

Daley, T.M., Miller, D.E., Dodds, K., Cook, P. & Freifeld, B.M., 2016. Field testing of modular borehole monitoring with simultaneous distributed acoustic sensing and geophone vertical seismic profiles at Citronelle, Alabama. *Geophysical Prospecting*, **64**, 1318–1334. doi:10.1111/1365-2478.12324

Dean, T., Cuny, T. & Hartog, A.H., 2017. The effect of gauge length on axially incident P-waves measured using fibre optic distributed vibration sensing: Gauge length effect on incident P-waves. *Geophysical Prospecting*, **65**, 184–193. doi:10.1111/1365-2478.12419

Department of Earth and Environmental Sciences, Geophysical Observatory, University of Munchen, 2001. BayernNetz (BH) seismic network. *International Federation of Digital Seismograph Networks*. doi:10.7914/SN/BW

Dussel, M., Lüschen, E., Thomas, R., Agemar, T., Fritzer, T., Sieblitz, S., Huber, B., *et al.*, 2016. Forecast for thermal water use from Upper Jurassic carbonates in the Munich region (South German Molasse Basin). *Geothermics*, **60**, 13–30. doi:10.1016/j.geothermics.2015.10.010

Ende, M.P.A. van den & Ampuero, J.-P., 2021. Evaluating seismic beamforming capabilities of distributed acoustic sensing arrays. *Solid Earth*, **12**, 915–934, Copernicus GmbH. doi:10.5194/se-12-915-2021

Eshelby, J.D. & Peierls, R.E., 1957. The determination of the elastic field of an ellipsoidal inclusion, and related problems. *Proceedings of the Royal Society of London. Series A. Mathematical and Physical Sciences*, **241**, 376–396, Royal Society. doi:10.1098/rspa.1957.0133

Farquharson, N., Schubert, D.A. & Steiner, U., 2016. Geothermal Energy in Munich (and Beyond) A Geothermal City Case Study, 8.

Feigl, K., Parker, L., Patterson, J., Reinisch, E.C., Nayak, A., Zeng, X., Cardiff, M.A., *et al.*, 2018. Overview of Results and Lessons Learned from the PoroTomo project at Brady Hot Springs, Nevada: Poroelastic Tomography by Adjoint Inverse Modeling of Data from Seismology, Geodesy, and Hydrology, Vol. 2018, pp. H31C-06, Presented at the AGU Fall Meeting Abstracts. Retrieved from https://ui.adsabs.harvard.edu/abs/2018AGUFM.H31C..06F

Feigl, K., Reinisch, E., Patterson, J., Jreij, S., Parker, L., Nayak, A., Zeng, X., *et al.*, 2016. PoroTomo Natural Laboratory Horizontal and Vertical Distributed Acoustic Sensing Data, DOE Geothermal Data Repository; University of Wisconsin. doi:10.15121/1778858

Flinn, E.A., 1965. Signal analysis using rectilinearity and direction of particle motion. *Proc. IEEE*, **53**, 1874–1876. doi:10.1109/PROC.1965.4462

Forbriger, T., Karamzadeh, N., Azzola, J., Gaucher, E., Widmer-Schnidrig, R. & Rietbrock, A., 2025. Calibration of the Strain Amplitude Recorded with DAS Using a Strainmeter Array. *Seismological Research Letters*. doi:10.1785/0220240308

Hanks, T.C. & Kanamori, H., 1979. A moment magnitude scale. *Journal of Geophysical Research: Solid Earth*, **84**, 2348–2350. doi:10.1029/JB084iB05p02348

Hartmann, H., Tanner, D.C. & Schumacher, S., 2016. Initiation and development of normal faults within the German alpine foreland basin: The inconspicuous role of basement structures. *Tectonics*, **35**, 1560–1574. doi:10.1002/2016TC004176

Hartog, A.H., 2017. *An Introduction to Distributed Optical Fibre Sensors*, 1st edn, CRC Press. doi:10.1201/9781315119014

Haubrich, R.A., 1968. Array design. *Bulletin of the Seismological Society of America*, **58**, 977–991. doi:10.1785/BSSA0580030977

Isken, M.P., Vasyura-Bathke, H., Dahm, T. & Heimann, S., 2022. De-noising distributed acoustic sensing data using an adaptive frequency–wavenumber filter. *Geophysical Journal International*, **231**, 944–949. doi:10.1093/gji/ggac229

Iyer, H.M., 1968. Determination of Frequency-Wave-Number Spectra Using Seismic Arrays. *Geophys J Int*, **16**, 97–117. doi:10.1111/j.1365-246X.1968.tb00211.x

Johnson, D.H. & Dudgeon, D.E., 1993. *Array Signal Processing: Concepts and Techniques*, Facsimile Edition., Prentice Hall.

Jousset, P., Currenti, G., Schwarz, B., Chalari, A., Tilmann, F., Reinsch, T., Zuccarello, L., *et al.*, 2022. Fibre optic distributed acoustic sensing of volcanic events. *Nat Commun*, **13**, 1753. doi:10.1038/s41467-022-29184-w

Keil, S., Wassermann, J., Megies, T. & Kraft, T., 2023. Optimal Network Design for Microseismic Monitoring in Urban Areas - A Case Study in Munich, Germany. *Seismica*, **2**. doi:10.26443/seismica.v2i2.1030

Kennett, B.L.N., 2022. The seismic wavefield as seen by distributed acoustic sensing arrays: local, regional and teleseismic sources. *Proc. R. Soc. A.*, **478**, 20210812. doi:10.1098/rspa.2021.0812

Kraft, T., Mai, P.M., Wiemer, S., Deichmann, N., Ripperger, J., Kästli, P., Bachmann, C., *et al.*, 2009. Enhanced Geothermal Systems: Mitigating Risk in Urban Areas. *Eos, Transactions American Geophysical Union*, **90**, 273. doi:10.1029/2009EO320001

Kristeková, M., Kristek, J. & Moczo, P., 2009. Time-frequency misfit and goodness-of-fit criteria for quantitative comparison of time signals. *Geophysical Journal International*, **178**, 813–825. doi:10.1111/j.1365-246X.2009.04177.x

Kristekova, M., Kristek, J., Moczo, P. & Day, S.M., 2006. Misfit Criteria for Quantitative Comparison of Seismograms. *Bulletin of the Seismological Society of America*, **96**, 1836–1850. doi:10.1785/0120060012

Lellouch, A. & Biondi, B.L., 2021. Seismic Applications of Downhole DAS. *Sensors*, **21**, 2897, Multidisciplinary Digital Publishing Institute. doi:10.3390/s21092897

Lellouch, A. & Wetzler, N., 2025. Probing the Dead Sea Fault with the First Wireline-Free Hybrid DAS-Accelerometer Array in an Abandoned Well. *Seismological Research Letters*. doi:10.1785/0220250179

Lellouch, A., Yuan, S., Ellsworth, W.L. & Biondi, B., 2019. Velocity-Based Earthquake Detection Using Downhole Distributed Acoustic Sensing—Examples from the San Andreas Fault Observatory at Depth. *Bulletin of the Seismological Society of America*, **109**, 2491–2500. doi:10.1785/0120190176

Lentas, K., Bowden, D., Melis, N.S., Fichtner, A., Koroni, M., Smolinski, K., Bogris, A., *et al.*, 2023. Earthquake location based on Distributed Acoustic Sensing (DAS) as a seismic

array. *Physics of the Earth and Planetary Interiors*, **344**, 107109. doi:10.1016/j.pepi.2023.107109

Li, Yang, Perton, M., Gaite, B., Ruiz-Barajas, S. & Spica, Z.J., 2023. Near-surface characterization using distributed acoustic sensing in an urban area: Granada, Spain. *Geophysical Journal International*, **235**, 1849–1860. doi:10.1093/gji/ggad331

Li, Yingping, Karrenbach, M. & Ajo-Franklin, J.B., 2021. A Literature Review. in *Distributed Acoustic Sensing in Geophysics*, pp. 229–291, American Geophysical Union (AGU). doi:10.1002/9781119521808.ch17

Li, Z. & Zhan, Z., 2018. Pushing the limit of earthquake detection with distributed acoustic sensing and template matching: a case study at the Brady geothermal field. *Geophysical Journal International*, **215**, 1583–1593. doi:10.1093/gji/ggy359

Lindsey, N.J., Rademacher, H. & Ajo-Franklin, J.B., 2020. On the Broadband Instrument Response of Fiber-Optic DAS Arrays. *J. Geophys. Res. Solid Earth*, **125**. doi:10.1029/2019JB018145

Lior, I., Rivet, D., Ampuero, J.-P., Sladen, A., Barrientos, S., Sánchez-Olavarría, R., Villarroel Opazo, G.A., *et al.*, 2023. Magnitude estimation and ground motion prediction to harness fiber optic distributed acoustic sensing for earthquake early warning. *Sci Rep*, **13**, 424, Nature Publishing Group. doi:10.1038/s41598-023-27444-3

Lior, I., Sladen, A., Mercerat, D., Ampuero, J.-P., Rivet, D. & Sambolian, S., 2021. Strain to ground motion conversion of distributed acoustic sensing data for earthquake magnitude and stress drop determination. *Solid Earth*, **12**, 1421–1442. doi:10.5194/se-12-1421-2021

Lomax, A. & Curtis, A., 2001. Fast, probabilistic earthquake location in 3D models using oct-tree importance sampling. 955, Vol. 3, pp. 10–1007.

Lomax, A., Michelini, A. & Curtis, A., 2014. Earthquake Location, Direct, Global-Search Methods. in *Encyclopedia of Complexity and Systems Science*, pp. 1–33, ed. Meyers, R.A., Springer New York. doi:10.1007/978-3-642-27737-5_150-2

Lomax, A., Virieux, J., Volant, P. & Berge-Thierry, C., 2000. Probabilistic Earthquake Location in 3D and Layered Models. in *Advances in Seismic Event Location* Modern Approaches in Geophysics, Vol. 18, pp. 101–134, eds Thurber, C.H. & Rabinowitz, N., Springer Netherlands. doi:10.1007/978-94-015-9536-0_5

Luu, K., 2020. disba - PyPI. *disba 0.6.1*. Retrieved from https://pypi.org/project/disba/

Lv, H., Zeng, X., Chi, B., Zhang, G. & Thurber, C., 2023. Monitoring seismicity triggered by geothermal site shutdown with a surface DAS array at Brady Hot Springs. *Geophysical Journal International*, **235**, 1861–1871. doi:10.1093/gji/ggad333

Madariaga, R., 1976. Dynamics of an expanding circular fault. *Bulletin of the Seismological Society of America*, **66**, 639–666. doi:10.1785/BSSA0660030639

Markom, A.M., Saharudin, S. & Hisham, M.H., 2025. Systematic review of fiber-optic distributed acoustic sensing: advancements, applications, and challenges. *Optical Fiber Technology*, **94**, 104293, Elsevier BV. doi:10.1016/j.yofte.2025.104293

Megies, T. & Wassermann, J., 2014. Microseismicity observed at a non-pressure-stimulated geothermal power plant. *Geothermics*, **52**, 36–49. doi:10.1016/j.geothermics.2014.01.002

Morten, J.P., Heinloo, A., Evangelidis, C., Strollo, A. & Tilmann, F., 2025, March 18. Enhancing rapid earthquake location by integrating streaming DAS virtual stations. doi:10.5194/egusphere-egu25-9133

Munn, J.D., Coleman, T.I., Parker, B.L., Mondanos, M.J. & Chalari, A., 2017. Novel cable coupling technique for improved shallow distributed acoustic sensor VSPs. *Journal of Applied Geophysics*, **138**, 72–79. doi:10.1016/j.jappgeo.2017.01.007

Muñoz, F. & Soto, M.A., 2022. Enhancing fibre-optic distributed acoustic sensing capabilities with blind near-field array signal processing. *Nat Commun*, **13**, 4019. doi:10.1038/s41467-022-31681-x

Mykkeltveit, S., Åstebøl, K., Doornbos, D.J. & Husebye, E.S., 1983. Seismic array configuration optimization. *Bulletin of the Seismological Society of America*, **73**, 173–186. doi:10.1785/BSSA0730010173

Näsholm, S.P., Iranpour, K., Wuestefeld, A., Dando, B.D.E., Baird, A.F. & Oye, V., 2022. Array Signal Processing on Distributed Acoustic Sensing Data: Directivity Effects in Slowness Space. *JGR Solid Earth*, **127**, e2021JB023587. doi:10.1029/2021JB023587

Nayak, A., Ajo-Franklin, J., & the Imperial Valley Dark Fiber Team, 2021. Distributed Acoustic Sensing Using Dark Fiber for Array Detection of Regional Earthquakes. *Seismological Research Letters*, **92**, 2441–2452. doi:10.1785/0220200416

Nishimura, T., Emoto, K., Nakahara, H., Miura, S., Yamamoto, M., Sugimura, S., Ishikawa, A., *et al.*, 2021. Source location of volcanic earthquakes and subsurface characterization using fiber-optic cable and distributed acoustic sensing system. *Sci Rep*, **11**, 6319, Nature Publishing Group. doi:10.1038/s41598-021-85621-8

Paitz, P., Edme, P., Gräff, D., Walter, F., Doetsch, J., Chalari, A., Schmelzbach, C., *et al.*, 2021. Empirical Investigations of the Instrument Response for Distributed Acoustic Sensing (DAS) across 17 Octaves. *Bulletin of the Seismological Society of America*, **111**, 1–10. doi:10.1785/0120200185

Peterson, J.R., 1993. Observations and modeling of seismic background noise (No. 93–322). *Open-File Report*, U.S. Geological Survey. doi:10.3133/ofr93322

Porras, J., Pecci, D., Bocchini, G.M., Gaviano, S., De Solda, M., Tuinstra, K., Lanza, F., *et al.*, 2024. A semblance-based microseismic event detector for DAS data. *Geophysical Journal International*, **236**, 1716–1727, Oxford University Press (OUP). doi:10.1093/gji/ggae016

Reinsch, T., Thurley, T. & Jousset, P., 2017. On the mechanical coupling of a fiber optic cable used for distributed acoustic/vibration sensing applications—a theoretical consideration. *Meas. Sci. Technol.*, **28**, 127003, IOP Publishing. doi:10.1088/1361-6501/aa8ba4

Schultz, P.S. & Claerbout, J.F., 1978. VELOCITY ESTIMATION AND DOWNWARD CONTINUATION BY WAVEFRONT SYNTHESIS. *GEOPHYSICS*, **43**, 691–714. doi:10.1190/1.1440847

Schulz, R. & Jobmann, M., 1989. Hydrogeothermische Energiebilanz und Grundwasserhaushalt des Malmkarstes im Süddeutschen Molassebecken, Teilgebiet: Hydrogeothermik; Final Report. *Institut für Geowissenschaftliche Gemeinschaftsaufgaben (GGA): Hannover, Germany*, **Archive Number 105040**.

Schwarz, B., 2019. Coherent wavefield subtraction for diffraction separation. *GEOPHYSICS*, **84**, V157–V168. doi:10.1190/geo2018-0368.1

Schweitzer, J., Fyen, J., Mykkeltveit, S., Gibbons, S.J., Pirli, M., Kühn, D. & Kværna, T., 2012. Seismic Arrays. *New Manual of Seismological Observatory Practice 2 (NMSOP2)*, 6 mb, 80 pages, Deutsches GeoForschungsZentrum GFZ. doi:10.2312/GFZ.NMSOP-2_CH9

Seithel, R., Gaucher, E., Mueller, B., Steiner, U. & Kohl, T., 2019. Probability of fault reactivation in the Bavarian Molasse Basin. *Geothermics*, **82**, 81–90. doi:10.1016/j.geothermics.2019.06.004

Sidenko, E., Tertyshnikov, K., Gurevich, B., Isaenkov, R., Ricard, L.P., Sharma, S., Van Gent, D., *et al.*, 2022. Distributed fiber-optic sensing transforms an abandoned well into a permanent geophysical monitoring array: A case study from Australian South West. *The Leading Edge*, **41**, 140–148. doi:10.1190/tle41020140.1

Taner, M.T., Koehler, F. & Sheriff, R.E., 1979. Complex seismic trace analysis. *GEOPHYSICS*, **44**, 1041–1063. doi:10.1190/1.1440994

Taylor, H.F. & Lee, C.E., 1993, March 16. Apparatus and method for fiber optic intrusion sensing. Retrieved from https://patents.google.com/patent/US5194847A/en

Verdon, J.P., Horne, S.A., Clarke, A., Stork, A.L., Baird, A.F. & Kendall, J.-M., 2020. Microseismic monitoring using a fibre-optic Distributed Acoustic Sensor (DAS) array. *GEOPHYSICS*, 1–48. doi:10.1190/geo2019-0752.1

Wang, H.F., Zeng, X., Miller, D.E., Fratta, D., Feigl, K.L., Thurber, C.H. & Mellors, R.J., 2018. Ground motion response to an ML 4.3 earthquake using co-located distributed acoustic sensing and seismometer arrays. *Geophysical Journal International*, **213**, 2020–2036. doi:10.1093/gji/ggy102

Willis, M.E., Ellmauthaler, A., Wu, X. & LeBlanc, M.J., 2021. Important Aspects of Acquiring Distributed Acoustic Sensing (DAS) Data for Geoscientists. in *Geophysical Monograph Series*, 1st edn, pp. 33–44, eds Li, Yingping, Karrenbach, M. & Ajo-Franklin, J.B., Wiley. doi:10.1002/9781119521808.ch2

Yin, J., Zhu, W., Li, J., Biondi, E., Miao, Y., Spica, Z.J., Viens, L., *et al.*, 2023. Earthquake Magnitude With DAS: A Transferable Data-Based Scaling Relation. *Geophysical Research Letters*, **50**, American Geophysical Union (AGU). doi:10.1029/2023gl103045

Zhai, Q., Yin, J., Yang, Y., Atterholt, J.W., Li, J., Husker, A. & Zhan, Z., 2025. Comprehensive Evaluation of DAS Amplitude and Its Implications for Earthquake Early Warning and Seismic Interferometry. *JGR Solid Earth*, **130**, American Geophysical Union (AGU). doi:10.1029/2024jb030288

Zhan, Z., 2020. Distributed Acoustic Sensing Turns Fiber-Optic Cables into Sensitive Seismic Antennas. *Seismological Research Letters*, **91**, 1–15. doi:10.1785/0220190112

Zhirnov, A.A., Stepanov, K.V., Chernutsky, A.O., Fedorov, A.K., Nesterov, E.T., Svelto, C., Pnev, A.B., *et al.*, 2019. Influence of the Laser Frequency Drift in Phase-Sensitive Optical Time Domain Reflectometry. *Opt. Spectrosc.*, **127**, 656–663. doi:10.1134/S0030400X1910031X

Appendix

Appendix A: Additional pictures associated with the installation of the DAS 3D array

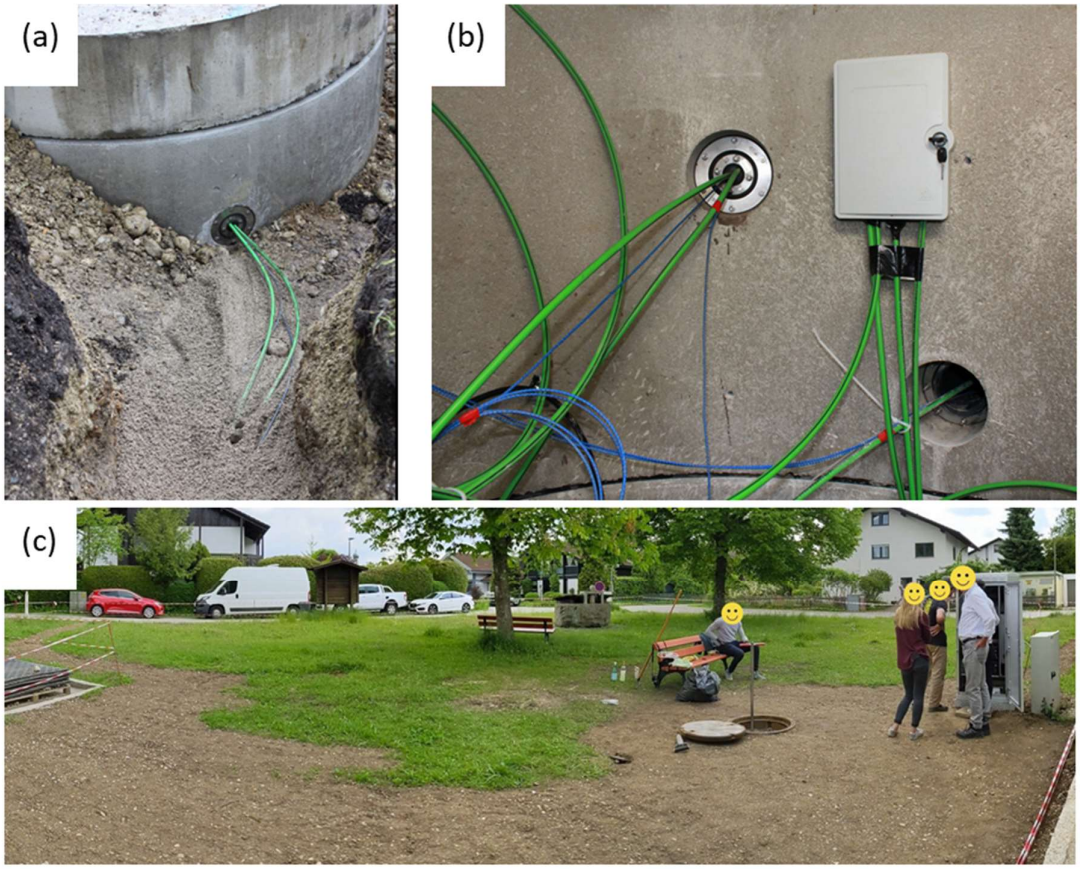

Figure A1: (a) FOC loops are routed through the vault before the trench is closed. (b): Picture of inside the vault, which contains the excess cables, the splicing boxes, and the Trillium Compact TC120 seismometer (not visible). (c): Overview of the small parc where the 3D-DAS array is installed, showing the entrance to the vault and the electrical cabinet used to store the devices.

Appendix B: Characterization of DAS sensing points

During installation of the FOC, the cable was geo-localized by a land surveyor. Length markers were collected along its trajectory, providing an estimate of the offset to the interrogation unit at each position along the cable.

To refine the spatial coordinates of the SP along the fiber, DAS data were recorded with a spatial sampling of 1 m and a gauge length of 2 m while local perturbations are applied to the cable. The experiment is illustrated in Figure B1, which shows DAS recordings as a function of offset from the interrogator unit. The color map shows the spectral energy. It is computed by applying a FFT to the signal recorded at each offset, and then integrating between 10 and 40 Hz, the main frequency band of the signal.

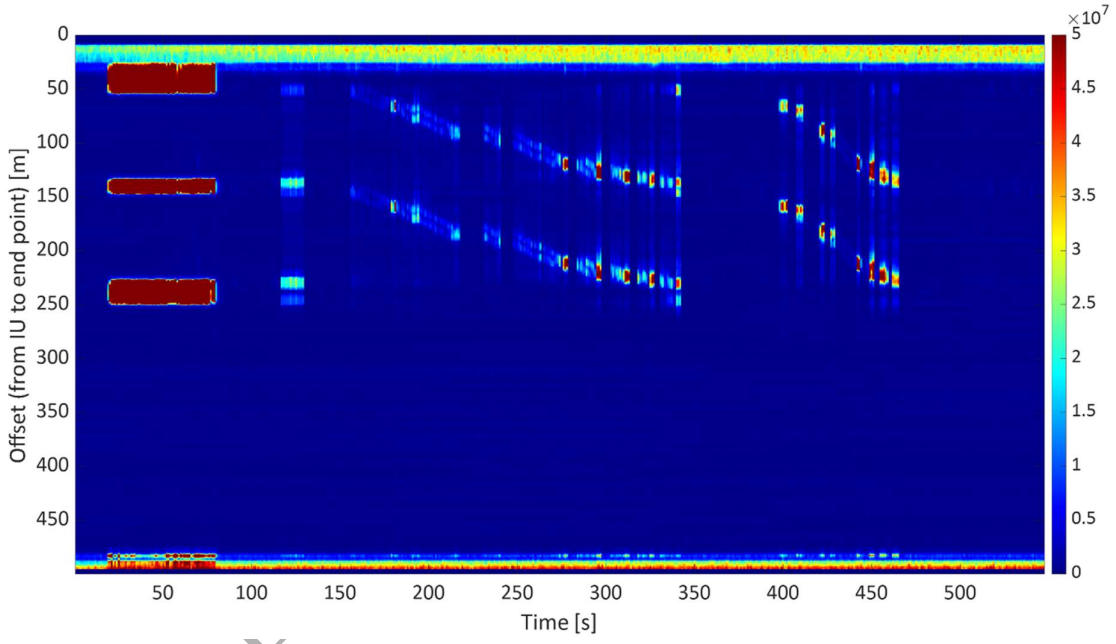

Figure B1: Evolution with time and offset along the cable of the spectral energy (color-scale) of the DAS data acquired while applying controlled perturbations and tap-tests around the surface loop.

The applied perturbations are used to identify reference positions along the fiber-optic cable. Before 150 s (see Figure B1), excess cable sections in the vault are activated, followed by

surface tap tests performed at the main corners of the surface loop. From this, we estimate the offsets at which the cable enters and exits the vault (see Figure B2 for the February 15 event example). The position of any SPs along the cable trajectory determined from the land survey is deduced using the known marker locations. When later using a coarser sampling and a higher gauge length, these positions can be determined by interpolating along the geosurveyed cable trajectory (Table B1 and B2). The traces from the surface loops and the vertical well are identified, which is illustrated in Figure B2 using the traces recorded during the 15 January seismic event.

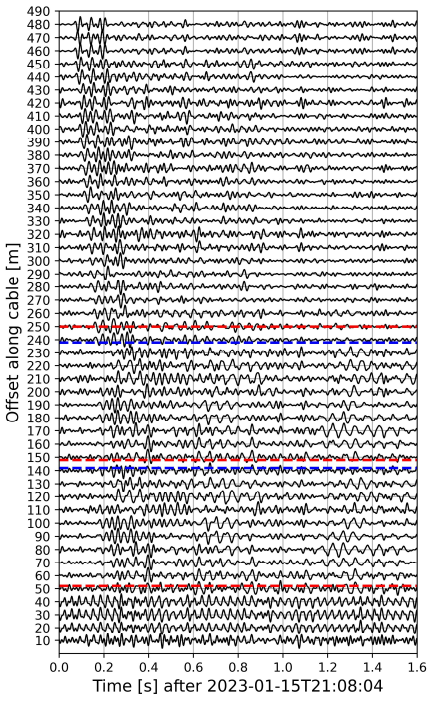

Figure B2: DAS strain-rate traces as a function of offset along the cable for the January 15 seismic event and after 5-50 Hz bandpass filtering. The blue and red dashed lines indicate the vault entry and exit points, delimiting the surface loops and the well section.

Table B1: Spatial coordinates of each SP around the surface loops (WGS 84 UTM32 coordinate system, EPSG:32632), offset with respect to the start of the FOC loop (i.e. at the exit of the vault) and recording azimuth.

Easting [m]	Northing [m]	Elevation [m]	Offset with respect to vault exit [m]	Recording azimuth
685469	5322569	611	2	N300°E
685460	5322571	611	8	N301°E
685457	5322562	611	12	N110°E
685459	5322552	611	18	N238°E
685466	5322545	611	22	N203°E
685476	5322546	611	28	N179°E
685486	5322549	611	32	N174°E
685486	5322558	611	38	N163°E
685480	5322564	611	42	N143°E
685474	5322565	611	48	N100°E
685466	5322570	611	52	N84°E
685458	5322567	611	58	N80°E
685458	5322558	611	62	N78°E
685461	5322548	611	68	N53°E
685470	5322546	611	72	N12°E
685480	5322548	611	78	N328°E
685487	5322552	611	82	N324°E
685481	5322559	611	88	N330°E

Table B2: Spatial coordinates of each SP located in the vertical well (WGS 84 UTM32 coordinate system, EPSG:32632), depth with respect to ground level and recording azimuth

Easting [m]	Northing [m]	Elevation [m]	Depth with respect to ground level [m]	Recording direction
4461917	5321381	603	8	vertical
4461917	5321381	593	18	vertical
4461917	5321381	583	28	vertical
4461917	5321381	573	38	vertical
4461917	5321381	563	48	vertical
4461917	5321381	553	58	vertical
4461917	5321381	543	68	vertical
4461917	5321381	533	78	vertical
4461917	5321381	523	88	vertical
4461917	5321381	513	98	vertical
4461917	5321381	503	108	vertical

4461917	5321381	493	118	vertical
4461917	5321381	483	128	vertical
4461917	5321381	473	138	vertical
4461917	5321381	463	148	vertical
4461917	5321381	453	158	vertical
4461917	5321381	443	168	vertical
4461917	5321381	433	178	vertical
4461917	5321381	423	188	vertical
4461917	5321381	413	198	vertical
4461917	5321381	403	208	vertical
4461917	5321381	393	218	vertical
4461917	5321381	373	238	vertical

Appendix C: DAS acquisition parameters

Table C1: DAS acquisition parameters

Parameter	**Value**
Pulse Rate Frequency	10 kHz
Sampling rate	500 Hz
Gauge length	20 m
Spatial sampling / inter-channel spacing along FOC	10 m
Temporal sampling	2.0 ms

Appendix D: Conversion from strain-rate to particle acceleration

Considering the propagation of a non-dispersive plane wave at location $\vec{r}$ and time t with a slowness-vector $\vec{s}$, particle displacement $\vec{u}$ can be expressed as a function of $\vec{U}$, its polarization and f, the shape of the wave or d'Alembert's solution to the wave equation.

$$\vec{u}(\vec{r},t) = \vec{U}\, f(\vec{s}\vec{r} - \vec{t}) \quad \text{(A1)}$$

Then, linear strain-rate $\dot{\varepsilon}_x(\vec{r},t)$ in any direction x, defined by its azimuth φ_x is:

$$\dot{\varepsilon}_x(\vec{r},t) = \frac{d}{dt}\frac{d}{dx}\, u_x(\vec{r},t) = \frac{d}{dt}\; U_x\, s_x\, f'\left(\vec{s}\vec{r} - \vec{t}\right) = {U_x}^2\, s_x\, f''(\vec{s}\vec{r} - \vec{t}) \quad \text{(A2)}$$

Likewise, the x-component of particle acceleration $a_x(\vec{r},t)$ is:

$$a_x(\vec{r},t) = \frac{d^2}{dt^2}u_x(\vec{r},t) = U_x{}^2 f''(\vec{s}\vec{r} - \vec{t}) \quad \text{(A3)}$$

Hence, the scaling relation between strain-rate and acceleration is given by Equation (A4):

$$\dot{\varepsilon}_x(\vec{r},t) = s_x \cdot a_x(\vec{r},t)\,, \quad \text{(A4)}$$

Or expressed as in Equation (1): $a_x(t) = {\dot{\varepsilon_x}(t)}/{s_x}$

Furthermore, with the *x*-direction being defined by an azimuth φ_x with respect to North, and the plane wave propagating in the direction $\phi - 180°$, with ϕ the back-azimuth, s_x can be expressed as a function of the horizontal component of slowness s_h:

$$s_x = s_h \cdot \cos(\phi - \varphi_x - 180°) \quad \text{(A5)}$$

Moreover, $a_x(t)$ can be expressed as a function of $a_N(t)$ and $a_E(t)$ (Equation A6), which in the present setting correspond to the temporal derivatives of the time series recorded by the BUCH.HLE and BUCH.HLZ channels, measuring particle velocity.

$$a_x(t) = a_E(t) \cdot \cos(\varphi_x) + a_N(t) \cdot \sin(\varphi_x) \quad \text{(A6)}$$

Substituting in Equation (A4) relates linear strain in the *x*-direction to these temporal derivatives, using the ray parameters of the wavefield:

$$\dot{\varepsilon}_x(t) = s_h \cdot \cos(\phi - \varphi_x - 180°) \cdot [a_E(t) \cdot \cos(\varphi_x) + a_N(t) \cdot \sin(\varphi_x)]$$

Appendix E: Time–frequency representation of the seismic signals from the January 15 event

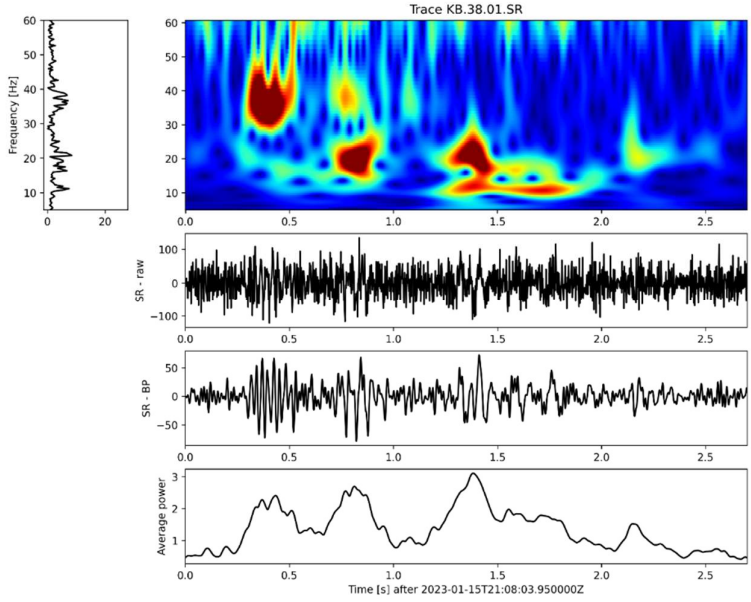

Figure E1: Time frequency representation of the signal using a Continuous Wavelet Transformation (CWT) in the frequency domain, based on a Morlet Wavelet and following (Kristekova *et al.* 2006; Kristeková *et al.* 2009)**. The corresponding time-series is displayed without (SR-raw) application of filter and after (SR-BP) applying a band-pass filter between 5 and 50 Hz. The bottom panel and the left panel show the average power computed from the spectrum over time and over frequency, respectively.**

Appendix F: Analysis of background strain-rate amplitudes and frequency characteristics

Located in a residential neighborhood, the recordings of the DAS 3D array are subject to anthropogenic noise, particularly when the park is frequented by residents. Figure F1a summarizes the SR variation over nine following days starting a Saturday (Jan. 7, 2023). Figure F1a shows the 95th percentile of the SR amplitudes recorded in consecutive 1-minute intervals, after applying a 5 to 50 Hz band-pass filter.

Figure F1b shows the variation along the cable of the temporal average of the measurement shown in panel (a). It shows that SPs located in the monitoring borehole collect less energy from the background disturbances than surface SPs. The reduction in SR-amplitudes in borehole recordings can also be seen qualitatively during daytime on January 10, for example.

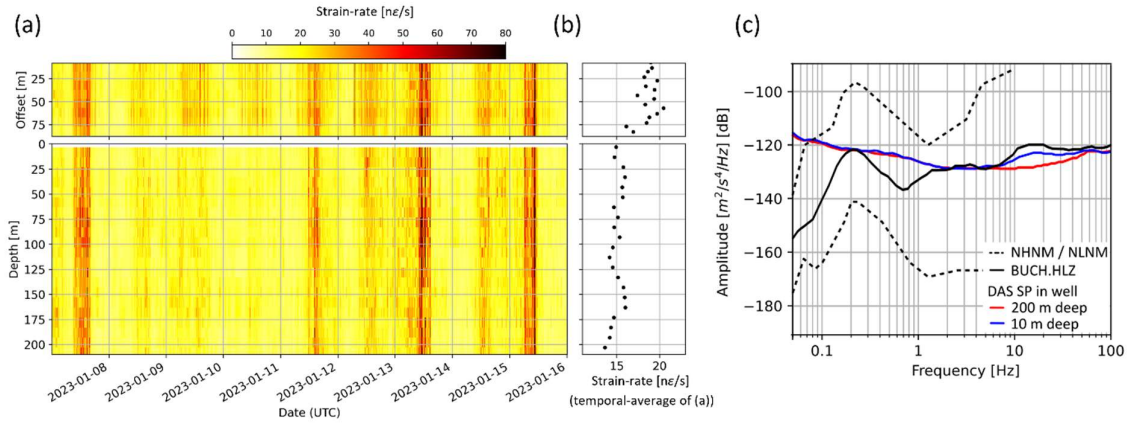

Figure F1: (a): SR amplitude recorded over the FOC during the week preceding the January 15 seismic event. The color scale shows the 95th percentile of all SR values recorded over 1-minute-long windows. The time-series are plotted according to the offset along the surface loop (top) and according to depth in the well section (bottom). (b): Spatial evolution along the optical fiber obtained after averaging the SR values presented in panel (a). (c): Comparison of median Power Spectral Densities (PSD) computed over the nine days displayed in panel (a). The spectrum of the vertical component of the BUCH seismometer (channel HLZ, black curve) is compared to the spectra from the DAS SP at a depth of 10 m

(blue) and 200 m (red) located in the vertical well. The dashed lines show the new high and new low noise models (Peterson 1993). Additional details about the computation of the DAS PSD are included in the main text.

Figure F1c shows median Power Spectral Densities (PSDs) computed with particle velocity from the broadband seismometer and SR from in-well DAS SPs. Individual PSDs are computed using 30 minutes long windows. The median PSD for the BUCH.HLZ channel lies between the low- and high-noise models, consistent with natural background levels. Assuming that background noise is predominantly composed of fundamental mode Rayleigh waves, the PSD computed from DAS SR recordings is multiplied by the phase velocity of the Rayleigh waves, obtained from the dispersion curve of fundamental mode Rayleigh waves. The latest is modeled with the *disba* Python library (Luu, 2020) using a 1D-velocity model characteristic of the study area. Figure F1c shows the signature of common-mode laser noise at low frequencies and no significant signature of the first microseismic peak on the DAS recordings. Between 10 and 100 Hz, we observe that the seismometer and the DAS capture significant energy, attributed to anthropogenic sources of noise. We note that median PSD values computed with DAS and seismometer data should be compared quantitatively with caution, as the conversion proposed above depends on the velocity model used to estimate dispersion curves. Above 10 Hz, the approach is influenced by shallow structures where 1D models often lack resolution. Comparing the PSD of the shallow (blue curve) and deep (red curve) DAS SPs, we also observe a maximum reduction of 5 dB at 8 Hz, suggesting also a reduction in the energy of background signals in the well section.

Appendix G: DAS strain-rate signals after applying a velocity-filter in the f-k domain

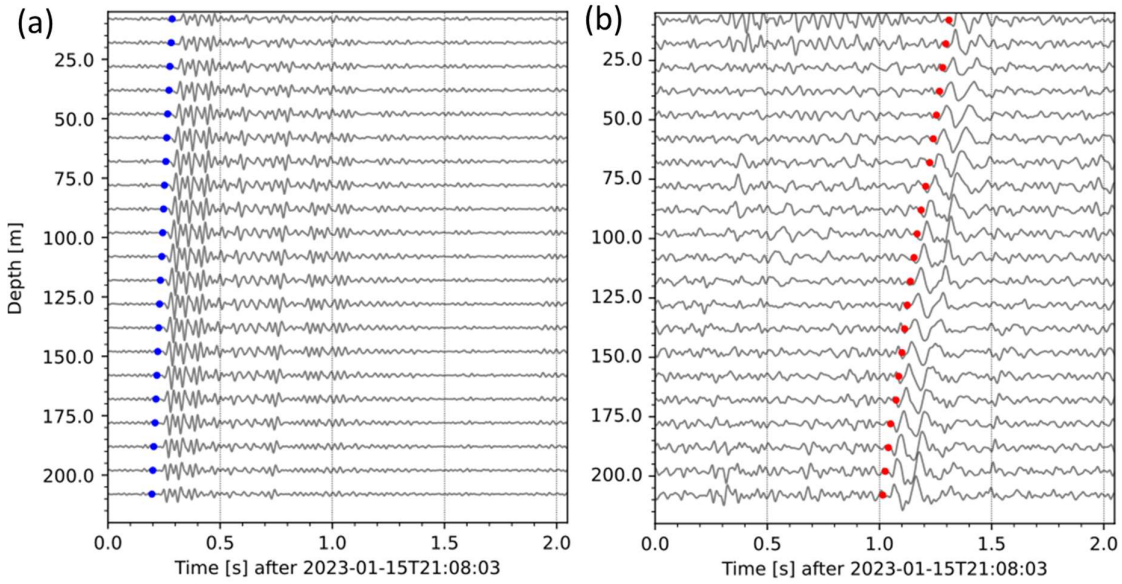

Figure G1: DAS strain-rate in the vertical well after applying a band-pass filter between 5 and 50 Hz and a narrow velocity-filter in the f-k domain, focusing (a) on the P-wave front between 1600 and 3500 m.s^{-1} and (b) on the S-wave front between 500 and 1600 m.s^{-1}.

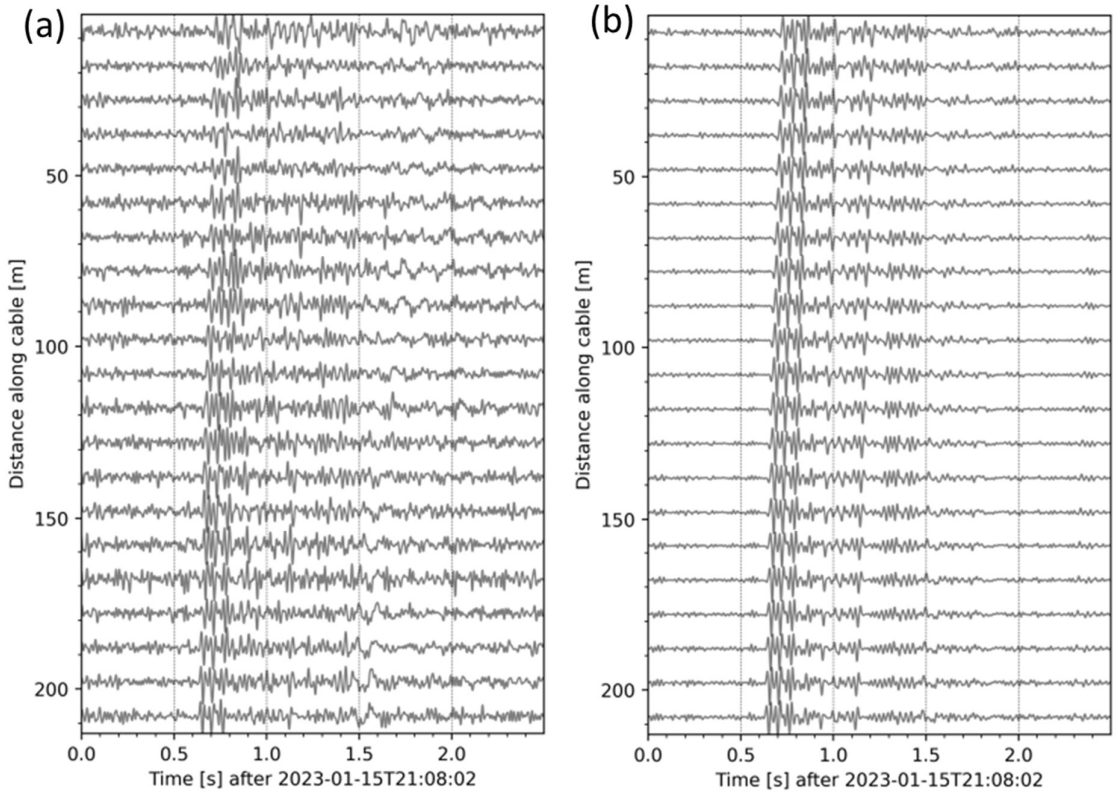

Figure G2: (a): DAS strain-rate in the well section after applying a band-pass filter between 5 and 50 Hz. (b). in-well DAS strain-rate after applying, in addition to (a), a narrow velocity-filter in the f-k domain between 1600 and 3500 m.s^{-1} (focus on the P-wave front) and weighting each time-depth data point by coherence, measured at each trace by a slant-stack approach.

Appendix H: Additional array responses

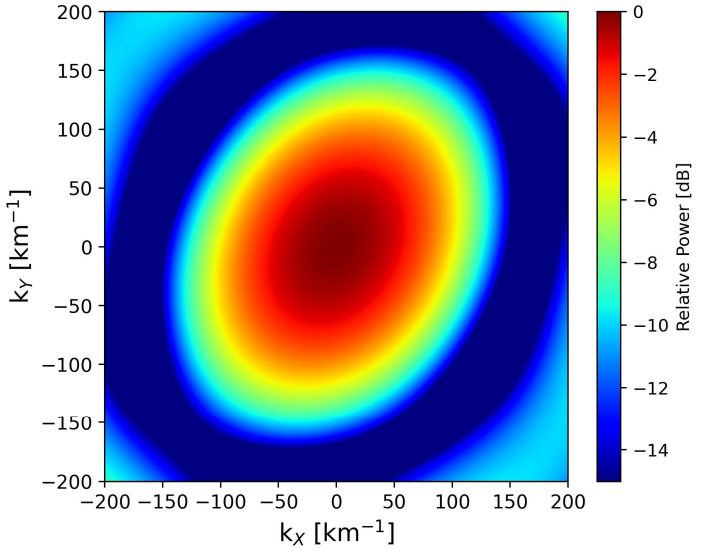

Figure H1: Relative power of the array response normalized with its maximum as a function of wavenumber difference.

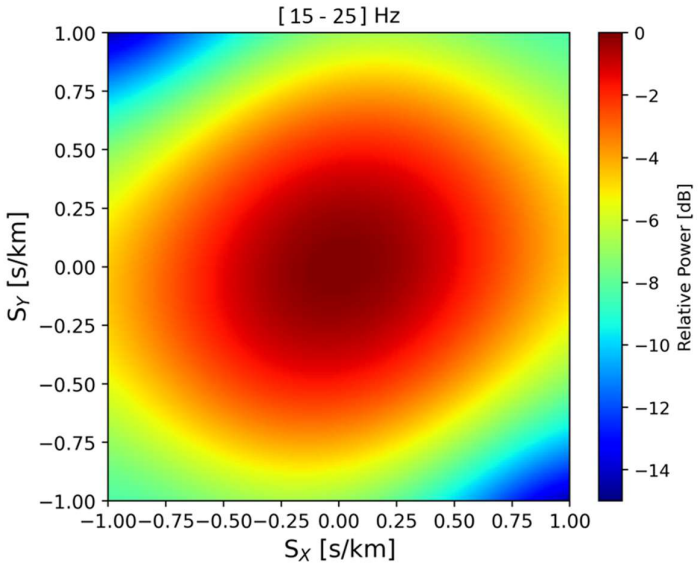

Figure H2: Relative power of the array response (in dB), normalized to its maximum, as a function of slowness differences within 15 and 25 Hz. The array response focuses on the (s_X, s_Y) plane, with s_Z = 0. The orientation of the SPs and the wave field directionality are accounted for, considering a BAZ of N80°E.